Improving the constraint on the M_w 7.1 2016 off-Fukushima shallow normal-faulting earthquake with the high azimuthal coverage tsunami data from the S-net wide and dense network: Implication for the stress regime in the Tohoku overriding plate

Tatsuya Kubota[1], Hisahiko Kubo[1], Keisuke Yoshida[2], Naotaka Y. Chikasada[1], Wataru Suzuki[1], Takeshi Nakamura[3], and Hiroaki Tsushima[4]

[1] National Research Institute for Earth Science and Disaster Resilience, Tsukuba, Japan.

[2] Graduate School of Science, Tohoku University, Sendai, Japan.

[3] Central Research Institute of Electric Power Industry, Abiko, Japan.

[4] Meteorological Research Institute, Japan Meteorological Agency, Tsukuba, Japan

Corresponding author: Tatsuya Kubota (kubotatsu@bosai.go.jp)

Key Points:

- Tsunamis due to the 2016 off-Fukushima shallow normal-faulting earthquake were observed by the S-net wide and dense pressure gauge network
- Use of the near-field and the high-coverage array significantly improved the constraint of the fault modeling of the 2016 earthquake
- Horizontal extensional stress predominant even before the 2011 Tohoku earthquake should be the main cause of the earthquake and tsunami

Abstract

Tsunamis with amplitudes of up to 40 cm, related to the M_w 7.1 normal-faulting earthquake off Fukushima, Japan, on November 21, 2016, were clearly recorded by a new offshore wide and dense ocean-bottom pressure gauge network, S-net, with high azimuthal coverage located closer to the focal area. We processed the S-net data and found some stations included the tsunami-irrelevant drift and step signals. We analyzed the S-net data to infer the tsunami source distribution. A subsidence region with a narrow spatial extent (~40 km) and a large peak (~200 cm) was obtained. The other near-coastal waveforms not used for the inversion analysis were also reproduced very well. Our fault model suggests the maximum stress drop across the fault plane of > ~10 MPa and the average of 4.2 MPa, whereas the shear stress increase along the fault caused by the 2011 Tohoku earthquake was only ~2 MPa. Past studies have suggested that horizontal compressional stress around this region switched to horizontal extensional stress after the Tohoku earthquake due to its stress perturbation. The present result, however, suggests that the horizontal extensional stress was locally predominant at the shallowest surface around the focal area even before 2011. The present study demonstrates that the S-net high-azimuthal-coverage pressure data provides a significant constraint on the fault modeling, which enables us to discuss the stress regime within the overriding plate at the offshore. Our analysis provides an implication for crustal stress states, which is important for understanding generation mechanisms of intraplate earthquakes.

Plain Language Summary

On November 21, 2016 (UTC), a large earthquake occurred within the continental plate off Fukushima, Japan, and a new seafloor tsunami network, S-net, recorded its tsunamis with much higher azimuthal coverage and with shorter epicentral distance than any of the previous networks. We analyzed the S-net data to reveal the rupture process of this earthquake. Our result explained all of the S-net data and the other tsunami network data very well. According to past studies, the continental plate in northeastern Japan was under horizontal compression before the 2011 Tohoku earthquake due to the pushing force by the subducting oceanic plate. However, our rupture modeling result suggested that the plate around the earthquake rupture area was horizontally stretched even before the Tohoku earthquake, so that the off-Fukushima earthquake occurred. Our study demonstrated that the S-net, which has high spatial coverage, makes it

possible to reveal the rupture model of offshore earthquakes, which was difficult in the past before S-net became available. The S-net will also enable us to discuss the impact of the Tohoku earthquake on the crustal stress, which is necessary for understanding the earthquake generation mechanics.

1 Introduction

In this decade, the coseismic rupture process of the 2011 Tohoku earthquake and its preseismic and postseismic processes have been investigated in detail (e.g., Hino, 2015; Kodaira et al., 2020; 2021; Lay, 2018; Uchida & Bürgmann, 2021; Wang et al., 2018). In response to the Tohoku earthquake, a new wide offshore deep-ocean observation network, Seafloor Observation Network for Earthquakes and Tsunamis along the Japan Trench (S-net), has been constructed off eastern Japan (Aoi et al., 2020; Kanazawa et al., 2016; Mochizuki et al., 2017; Uehira et al., 2016, Figure 1a). Recent studies have started to utilize S-net ocean-bottom seismometers to investigate the seismotectonics and geodynamics in the Tohoku subduction zone (Dhakal et al., 2021; Hua et al., 2020; Matsubara et al., 2019; Nishikawa et al., 2019; Sawazaki & Nakamura, 2020; Takagi et al., 2019, 2021; Tanaka et al., 2019; Uchida et al., 2020; Yu & Zhao, 2020). The S-net also incorporates ocean-bottom pressure gauges (OBPGs), which are expected to be utilized for tsunami forecasts (e.g., Aoi et al., 2019; Inoue et al., 2019; Mulia & Satake, 2021; Tanioka, 2020; Tsushima & Yamamoto, 2020; Wang et al., 2021; Yamamoto et al., 2016a; 2016b). The other potential contributions to the earth sciences of the S-net OBPG have also been demonstrated, such as understanding the wave propagation process in the ocean as well as the rupture process of subseafloor earthquakes (Kubota et al., 2020a; 2021; Saito & Kubota, 2020; Saito et al., 2021). The wide and dense network data of S-net will significantly broaden our understanding of the Tohoku subduction zone after the Tohoku earthquake.

On November 21, 2016, a major shallow normal-faulting earthquake occurred within the overriding plate off Fukushima Prefecture (20:59 UTC, M_w 6.9, 12 km, Global CMT [GCMT], https://www.globalcmt.org, Figure 1, hereafter referred to as the off-Fukushima earthquake). Compared with the GCMT centroid, its epicenter, as determined by Japan Meteorological Agency (JMA), was located ~20 km east to northeast (white star in Figure 1). Numerous aftershocks accompanied this earthquake (Figures 1b and 1c). It has been reported that the tsunamis associated with the off-Fukushima earthquake were observed by onshore and offshore tsunami networks (e.g., Gusman et al., 2017; Kawaguchi et al., 2017; Suppasri et al., 2017). However, these stations were located only on the shore-side from the focal area, and the source-station distances are large (Figure 1a). In contrast, the S-net OBPGs recorded tsunamis with much higher azimuthal coverage and with a closer distance to the focal area (~30 km, Figure 1a). Because of the much better station coverage of the S-net, the constraint on the initial sea height (tsunami source) estimation and the finite fault modeling of the off-Fukushima earthquake will be significantly increased, as compared with the previous datasets.

The normal-faulting mechanism of the off-Fukushima earthquake is similar to nearby shallow normal-faulting micro-seismicity within the overriding plate, with a tensile axis (σ_3) oriented in basically the east-west direction, which significantly increased after the Tohoku earthquake (Figures 1d–1f, e.g., Asano et al., 2011; Hardebeck & Okada, 2018; Hasegawa et al., 2012; Tanaka et al., 2014; Wang et al., 2019; Yoshida et al., 2012). This increase in the normal-faulting seismicity is considered to be related to the significant stress perturbation by the Tohoku earthquake, which switched the intraplate stress regime from horizontal compression to horizontal extension (e.g., Hasegawa et al. 2012). If we can obtain a detailed fault model of the off-Fukushima earthquake, then the quantitative relationship between the crustal stress released during the off-Fukushima earthquake (i.e., stress drop) and the stress increase due to the 2011 Tohoku earthquake can be discussed. Because the generation of earthquakes is very closely related to the process of the stress accumulation and release, this quantitative comparison of the stresses is essential to deepen our understanding of the temporal change of the crustal stress state associated with the Tohoku earthquake and our knowledge of the generation mechanisms of the subseafloor crustal earthquakes related to the offshore megathrust earthquake, which may excite the significant tsunamis to cause a severe damage to the coast.

Because of the tsunamis' much smaller propagation velocity than that of seismic waves, the tradeoff between the earthquake source dimension and the rupture velocity is much smaller (Kubota et al. 2018a). In addition, shallow earthquakes generally excite tsunamis more efficiently than deep earthquakes (Kubota et al. 2019). So tsunami data have a strong advantage in the robust constraint on the fault slip extent and slip amount of the 2016 off-Fukushima earthquake, leading to the robust constraint on the stress drop. In the present study, therefore, we estimate the detailed finite fault model of the off-Fukushima earthquake using the S-net OBPG data. From the finite fault model, we also attempt to examine the normal-faulting stress state within the crust around the off-Fukushima earthquake and its relationship with the Tohoku earthquake, based on the stress drop estimation from the finite fault model. Section 2 describes the dataset used in this study, and Section 3 summarizes the feature in the S-net OBPG data. The spatial distribution of the initial sea surface height (tsunami source) and the finite fault model of the off-Fukushima earthquake are estimated in Sections 4 and 5, respectively. Section 6 examines the relationship between the Tohoku earthquake and the stress regime around the focal area. Section 7 concludes the present study.

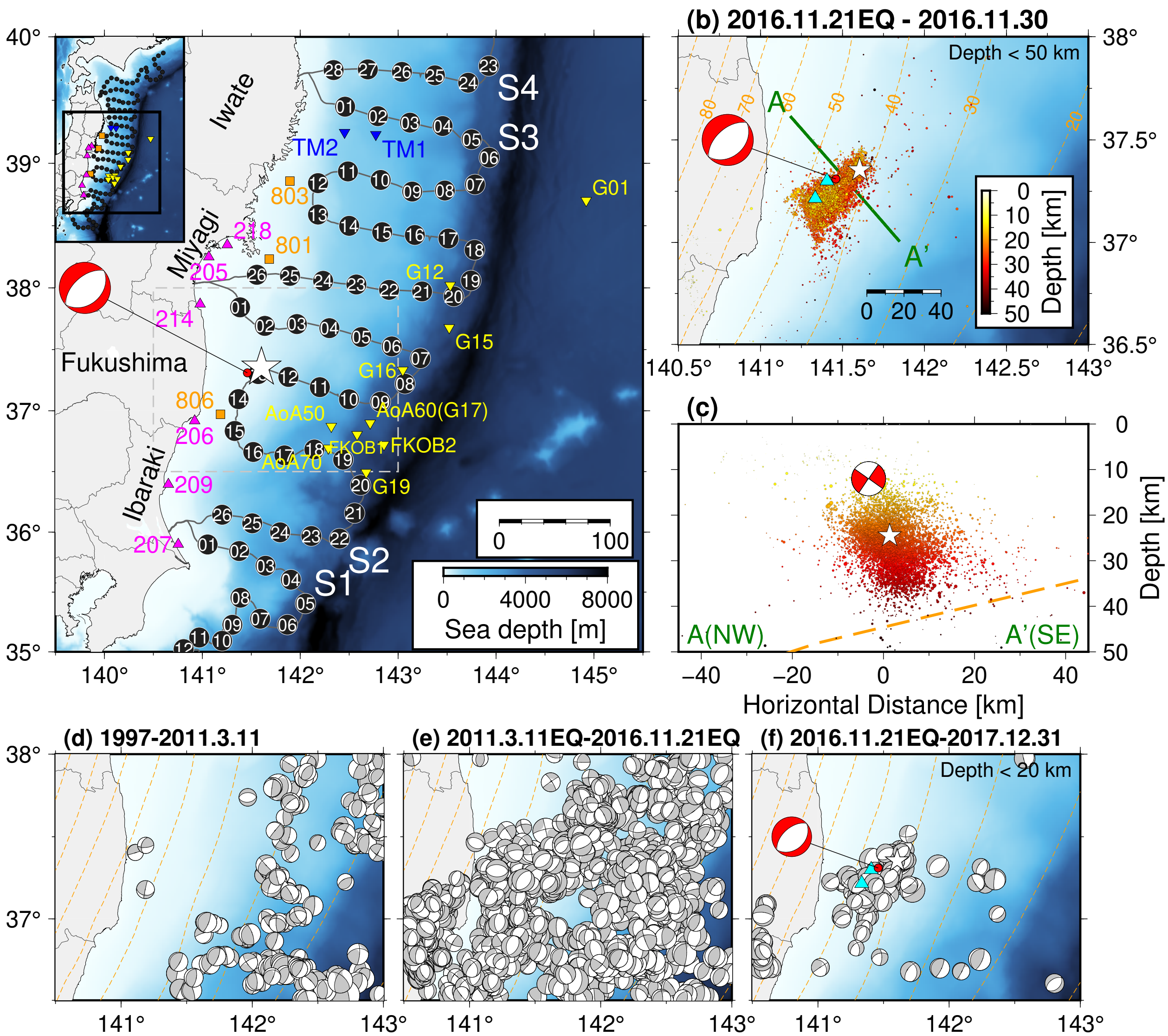

Figure 1. (a) Location map of the present study. Locations of the tsunami stations are shown by colored symbols (black circle: S-net OBPG, blue inverted triangle: ERI OBPG, yellow inverted triangle: Tohoku University OBPG, orange square: NOWPHAS GPS buoy, pink triangle: NOWPHAS wave gauge). The epicenter (white star) and the CMT solution (red) of the off-Fukushima earthquake are taken from JMA and GCMT, respectively. (b) Enlarged view of the rectangular area drawn by gray lines in Figure 1a. Aftershocks during about one week as determined by JMA are shown (color denotes its depth). Orange contours show the depth of the subducting plate interface (Nakajima & Hasegawa, 2006). The locations of fresh seafloor cracks

found by the JAMSTEC survey are shown by blue triangles. (c) Vertical cross section along line A-A' in Figure 1b. (d–f) The F-net fault mechanisms (Fukuyama et al., 1998) at depths shallower than 20 km, (d) before the Tohoku earthquake, (e) between the Tohoku earthquake and the off-Fukushima earthquake, and (f) after the off-Fukushima earthquake.

2 Tsunami dataset

The present study used the S-net OBPG data (black circles in Figure 1a, Wang & Satake, 2021). Although S-net now consists of 150 observatories (Aoi et al., 2020), 25 of these observatories, located at the outer-trench region, were not installed when the off-Fukushima earthquake occurred. Each observatory is equipped with absolute pressure sensors manufactured by Paroscientific, Inc. (e.g., Polster et al., 2009; Watts & Kontoyiannis, 1996). Two pressure sensors are equipped in each observatory for redundancy. The sensors are not directly exposed to the seawater, but rather are sealed in a metal housing filled with oil. The metal housing is further sealed in a metal cylindrical vessel filled with oil. The external pressure is transferred to the pressure sensor inside via a diaphragm made of hard rubber. See Aoi et al. (2020) for more details.

In addition to S-net, we use other OBPGs to evaluate the modeling resolution. We use the OBPGs off Iwate Prefecture installed by the Earthquake Research Institute (ERI) of the University of Tokyo (blue inverted triangles in Figure 1a, Gusman et al., 2017; Kanazawa & Hasegawa, 1997) and the OBPGs off eastern Japan installed by Tohoku University (yellow inverted triangles, Hino et al., 2014; 2021). We also use the offshore GPS buoys (orange squares) and wave gauges (pink triangles) of the Nationwide Ocean Wave information network for Ports and HArbourS [NOWPHAS] (Kawaguchi et al., 2017; Nagai et al., 1998).

3 Fundamental feature of the S-net OBPGs: Tsunami-irrelevant pressure signals

In order to investigate the fundamental feature of the S-net OBPG signals, we first process the OBPG data. We decimate the original 10 Hz data to 1 Hz (Figures 2a–2i). We then subtract the theoretical tide calculated by the model of Matsumoto et al. (2000) and apply a low-pass filter with a cutoff of 100 s in both forward and backward directions, to reduce the high-frequency seismic wave signals (Figure 2j–2r).

Figures 2a–2i show the 1-Hz-sampling pressure waveforms. The high-frequency fluctuations related to the seismic waves and ocean-acoustic waves (e.g., Kubota et al., 2020b) are observed. The gradual pressure increases related to the ocean tide are also observed, although some traces show different trends. The pressure changes recorded by the two sensors equipped in the same observatory (black and gray lines) are very similar to each other. The difference between these two traces (red lines) is around zero, although some stations have offsets in the differences. At station S2N13, which is located just above the focal area of the off-Fukushima earthquake, no seismic or tsunamis signals were recorded, although the co-equipped seismometer correctly recorded the ground shaking of this earthquake (Dhakal et al., 2021; Takagi et al., 2019; see also https://www.hinet.bosai.go.jp/topics/off-fukushima161122/?m=snet, in Japanese). This may suggest that the pressure observation part at S2N13 observation node did not work correctly. We note that the instrument at this site was replaced in 2020 (https://www.seafloor.bosai.go.jp/notice/notice_200414_1.pdf, in Japanese), and this site recorded tsunamis related to a M_{JMA} 7.3 earthquake on 13 February 2021 (https://www.hinet.bosai.go.jp/topics/off-fukushima210213/?m=others, in Japanese).

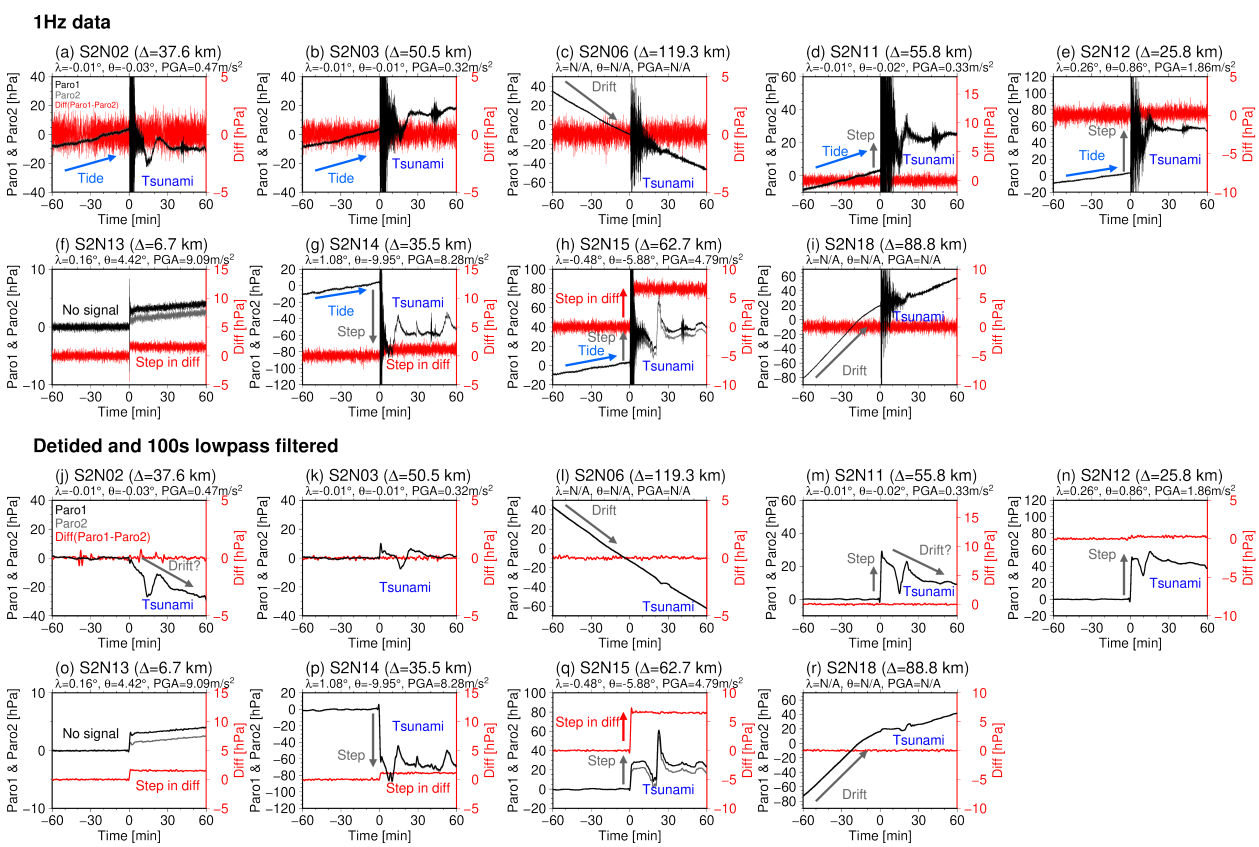

Figure 2. (a–i) The 1-Hz ocean-bottom pressure waveforms for stations (a) S2N02, (b) S2N03, (c) S2N06, (d) S2N11, (e) S2N12, (f) S2N13, (g) S2N14, (h) S2N15, and (i) S2N18. Black and gray traces denote the waveforms from each of the pressure sensors. Red traces denote the difference between the two sensors. Note that the vertical scale for the difference waveforms is different in each subfigure. The dominant signals are indicated by arrows and text. The epicentral distance Δ measured from the JMA epicenter, and the tilt change λ, rotation angle change θ, and peak ground acceleration (PGA) values measured by the co-equipped accelerometer (Takagi et al., 2019) are also shown. (j–r) Ocean-bottom pressure waveforms after data processing for the stations.

Although the tsunamis are confirmed in the lowpass-filtered S-net OBPG waveforms (Figures 2j–2r), we also recognize some signals irrelevant to the tsunamis, such as the large drift components (e.g., > ~50 hPa/hour, S2N06 and S2N18). If these drifts are caused by a vertical movement due to the postseismic deformation or the unstable slow sliding of the sensor, the vertical movement rate will be ~50 cm/hour (1 hPa pressure change is approximated as 1 cm displacement). This is too unrealistic. In addition, these drift features are also confirmed in some of the other sites at water depth shallower than 1500 m, in which the instruments are buried about one meter beneath the seafloor (Aoi et al., 2020). Therefore, these drifts are not caused by the real movement, but it might be possible to be caused by the mechanical reason. Some previous studies reported that the Paroscientific pressure sensors contain instrumental drift with rates of ~8.8 hPa/year (Inazu & Hino, 2011; Polster et al. 2009; Watts & Kontoyiannis, 1996), although this previously-reported rates are much smaller. It is also incomprehensible that the drift rates are completely identical in the sensor pair, although the instrumental drift must be individually different in each sensor. Therefore, we do not consider the cause of these drifts to be the one previously reported. Although we cannot identify the reason for these drifts, we suspect the observation system of the S-net may be relevant. The observation system of the S-net observation node, which includes not only the OBPG sensors but also other instruments such as seismometers, a power supply unit, and a real-time data transmitting unit (Aoi et al., 2020), is much more complicated than the ordinary offline pop-up pressure observation (e.g., Hino et al., 2014).

In addition, abrupt steps at the origin time are observed at some OBPGs, particularly at S2N11, S2N12, S2N14, and S2N15. The step is also observed at S2N13, where no tsunami signals were recorded. If we consider the pressure offset changes as a result of the seafloor vertical movement, these pressure changes correspond to a seafloor vertical displacement of ~30–60 cm (1 hPa pressure change is approximated as 1 cm vertical movement). Considering the source-station distances, these displacements seem too large compared with those expected from typical M~7 earthquakes. Furthermore, even if the OBPGs are located inside the focal area where the vertical displacement is large, the ocean-bottom pressure, or the seawater column height above the OBPG, cannot change so abruptly because both seafloor and sea-surface simultaneously move vertically during tsunami generation (e.g., Tsushima et al. 2012). Therefore, these steps are unlikely to be caused by the seafloor permanent displacement. Similar pressure steps were also recorded by the S-net and the other OBPG networks during the past earthquakes (Kubota et al., 2018b; 2020a; Wallace et al. 2016), which are not considered to be related to the tsunami or the seafloor crustal deformation.

It has been reported that outputs of Paroscientific pressure sensors strongly depend on its orientation relative to the direction of gravity (Chadwick et al., 2006). Thus, the step signals might be caused by the rotation of the pressure sensor. According to Chadwick et al. (2006), the rotation angle change of the pressure sensor of θ ~10° roughly corresponds to the apparent pressure offset change of up to ~10 hPa. Takagi et al. (2019) analyzed the co-equipped accelerometer during the off-Fukushima earthquake and found that some observatories near the epicenter rotated associated with large seafloor ground motion (Figure 2). However, comparing the rotation angles at some near-source stations (e.g., $\theta = 0.86°$ at S2N12 and 9.95° at S2N14, Takagi et al., 2019), the observed pressure steps were extremely large (> ~50 hPa). Furthermore, considering that the sensitivity to the rotation angle must be different in each sensor, it is quite strange that the amounts of the pressure step in two pressure sensors are almost identical. We also confirm that the pressure steps in the two pressure sensors are different at some stations where the large rotation was observed (e.g., S2N13, S2N15), leading to the steps around the focal time in the difference traces between the two sensor outputs (red lines in Figure 2). Taking these points into account, we consider that the dominant cause of the pressure steps is not the response to the sensor rotation as reported by Chadwick et al. (2006), and the difference in the steps between the two sensors may be due to the difference in the response to the rotation angle.

Although more detailed investigation is needed, we suspect the strong shaking of the instrument due to the seismic motion might have mainly caused these steps, which may affect the observation system of S-net, such as the transferring system of the external pressure to the sensor inside of the metal housing. As a summary of this section, we emphasize that we must be careful to analyze the OBPG data to distinguish whether such signals are real or are artifacts related to the drift or offset, although the S-net OBPGs clearly recorded the tsunamis due to the 2016 off-Fukushima earthquake.

4 Tsunami source modeling

4.1 Modeling procedure

In this section, we analyze the S-net data to estimate the spatial distribution of initial sea-surface height (tsunami source) of the off-Fukushima earthquake and to investigate how the S-net OBPGs provide better constraint. In order to reduce the long-period tsunami-irrelevant drift signals as well as the short-period seismic wave components, we apply the bandpass filter with passbands of 100–3,600 s (Figure 3b). We here briefly describe the procedure for the tsunami source modeling. The full details are shown in Text S1.

We distribute the unit source elements of the seafloor vertical displacement with horizontal spatial intervals of 2 km, in an area of 50 km × 50 km (rectangular area in Figure 3a). To calculate pressure change waveforms excited by each unit source element (i.e., the Green's functions) we simulate tsunamis by solving a linear dispersive tsunami equation (Saito, 2019; Saito et al., 2010). We use the JTOPO30 bathymetry data with a spatial resolution of 30 arcsec, interpolating the spatial interval of 1 km. We assume the vertical displacement of the unit sources is equal to the initial sea-surface height change and the displacement occurs instantaneously at time $t = 0$ s. After the tsunami simulation, we calculate the pressure change p at each OBPG location by subtracting the seafloor vertical movement from the sea-surface height change (Tsushima et al., 2012), $p = \rho_0 g_0 (\eta - u_z)$ (ρ_0: seawater density, g_0: gravitational acceleration, η: sea-surface height change, and u_z: seafloor vertical displacement). We here suppose $\rho_0 \sim 1.02$ g/cm^3 and $g_0 = 9.8$ m/s^2, so that 1 cm change of seawater column height ($\eta - u_z$) equals to 1 hPa pressure change (i.e., $\rho_0 g_0 = 1$ hPa/cm). We finally apply the same bandpass filter to the simulated waveform as that applied to the observation.

In the inversion analysis, we use the time-derivative waveforms of the bandpass-filtered pressure ($\partial p/\partial t$, the method of Kubota et al. (2018b)), because the time-derivative can reduce the artefacts due to the tsunami-irrelevant steps, which becomes the impulse and thus does not contain the offset change. The data time window used for the modeling is determined based on the visual inspection which includes the main part of the tsunami (listed in Table S1, blue traces in Figure 3c). The goodness of the estimated source is evaluated using the variance reduction (VR):

$$\mathrm{VR} = \left(1 - \frac{\sum_i \left(d_i^{\mathrm{obs}} - d_i^{\mathrm{cal}}\right)^2}{\sum_i \; {d_i^{\mathrm{obs}}}^2}\right) \times 100\ (\%) \tag{1}$$

where d_i^{obs} and d_i^{cal} are the i-th observed and calculated data, respectively. We impose the smoothing constraint for the inversion, and its weight is determined based on the trade-off between the weight and the VR (Figure S1) to avoid both overfitting and oversmoothing.

4.2 Results

Figure 3 shows the results of the inversion. A subsidence with a horizontal extent of ~40 km × ~20 km, having a sharp peak near the GCMT centroid, was obtained (Figure 3a). The direction of the northeast-southwest extents of the subsidence is consistent with the GCMT strike angle of 49°. The western edge of the subsidence region is consistent with the locations where the seafloor displacements of 1–2 m and fresh seafloor cracks were found by a seafloor bathymetry survey just after the off-Fukushima earthquake conducted by Japan Agency for Marine-Earth Science and Technology [JAMSTEC] (blue triangles in Figure 3a). The time derivatives of the S-net pressure waveforms were well reproduced (VR = 95.7%, Figure 3c). Except for the steps just after the focal time at some near-source OBPGs, the observed pressure is also well explained (Figure 3b). The waveforms recorded at the other tsunami stations (Figure 1a) are also reproduced surprisingly well (Figures 3d–3g), even though they were not used for the inversion. This suggests that the use of the S-net data provides good spatial resolution of the tsunami source, and thus it is expected that we can obtain a reliable fault model. Note that the later arrivals in some stations (e.g., ~100 min at TM1 and TM2) are not well reproduced, which are caused by the coastal-reflections (Gusman et al., 2017). This is probably because the spatial resolution of the coastal shape from the topography data in our simulation is not sufficient to reproduce the reflected tsunami waves, and the high-resolution bathymetry data is necessary (Gusman et al., 2017; Kubota et al., 2018a).

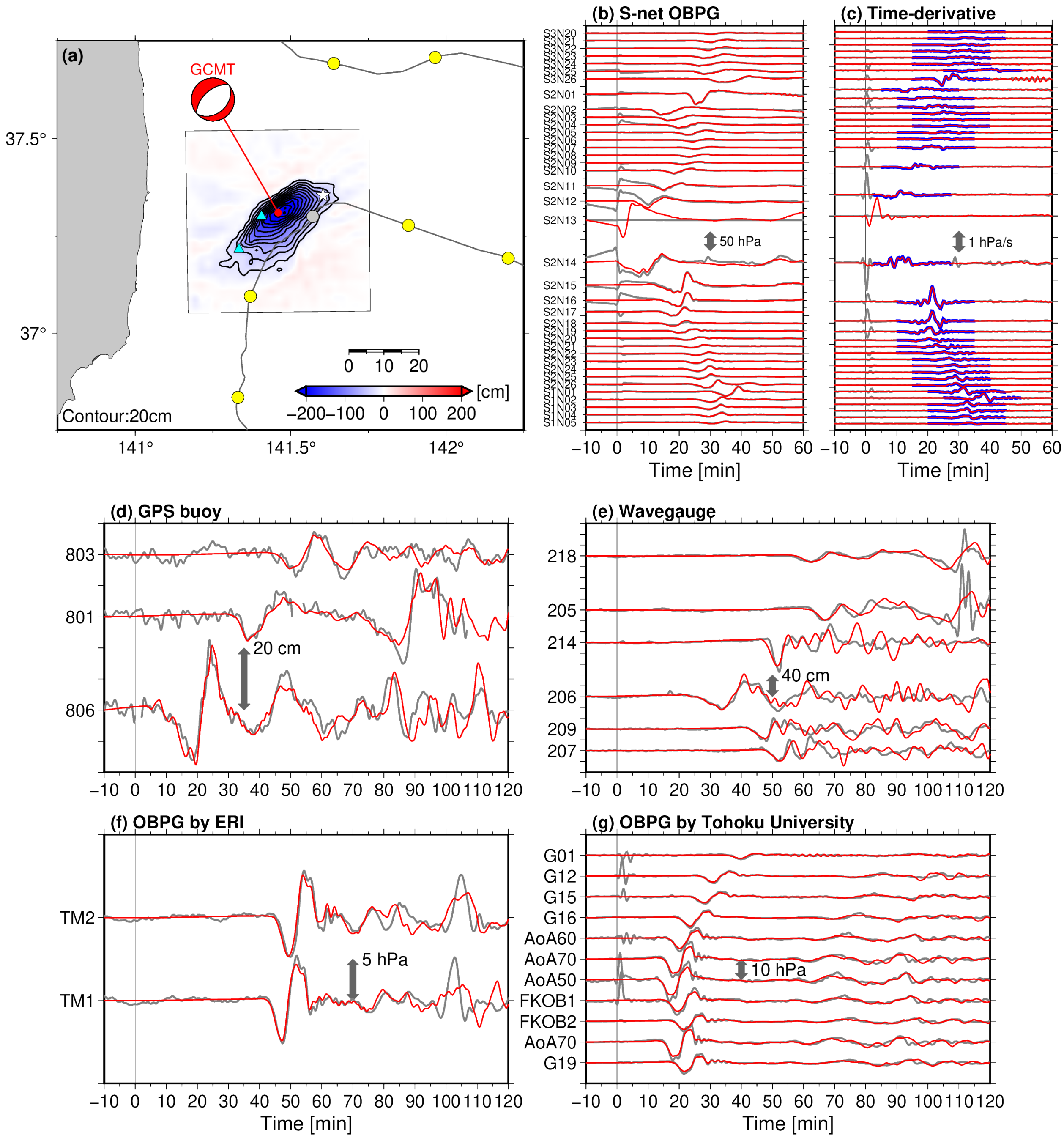

Figure 3. Results of the tsunami source inversion. (a) Spatial distribution of the tsunami source. Contour lines denote the subsided region with intervals of 20 cm. The white star is the JMA epicenter, and blue triangles denote the location of the seafloor survey, where fresh surface

cracks were found. The yellow and gray circles show the S-net OBPGs used or not used, respectively, for inversion analysis. Comparisons of (b) the pressure waveforms and (c) the time-derivative waveforms. The gray and red traces denote the observed waveforms and simulated waveforms from the tsunami source model. Traces marked by blue lines denote the time window used for the inversion analysis. (d–g) Waveform comparisons for the other networks, for (d) NOWPHAS Near-coastal GPS buoys, (e) NOWPHAS wave gauges, (f) OBPGs installed by ERI, and (g) OBPGs installed by Tohoku University. At station 801, the waveforms during the data missing are not drawn. See Figure 1 for station locations.

In the inversion, we used the time-derivative waveforms of the pressure to reduce the artefacts attributed to the tsunami-irrelevant pressure components (Kubota et al., 2018b). In order to see how well this method reduced the artefacts, we also conduct the additional inversion using the original pressure waveforms, instead of its time-derivative waveforms (Figure S2). The weight of the smoothing is also determined based on the VR between the observed and simulated pressure waveforms (Figure S1). As a result, the distribution of the tsunami source is fundamentally similar to the original distribution (VR = 87 %), although a significant artificial uplift of > 60 cm is estimated around S2N14 where the large step was recorded. Related to this artefact, the artificial pressure step irrelevant to the tsunami at S2N14 (see Section 3) was reproduced, whereas that was not reproduced when using the time-derivative waveforms. In order to avoid the artefact due to the tsunami-irrelevant step signals, the inversion using the time-derivative waveforms worked well.

We compare the tsunami source model estimated by the present study with the models obtained using the tsunami data except for the S-net data (Figure S3, Table 1). The horizontal location and spatial extent of the subsided region of our tsunami source model roughly correspond to those obtained by the previous studies. However, the amount of the maximum subsidence was much larger than the previous models and the locations of the peak subsidence of tsunami source are slightly different from each other. Our tsunami source model had a maximum subsidence of ~238 cm, whereas the two models obtained from the far-field tsunami data (Adriano et al., 2018; Gusman et al. 2017) underestimated the subsidence (~180 cm and ~130 cm, respectively, Table 1). The subsidence peak of our model was located ~10 km southeast and east of the models by Gusman et al. (2017) and Adriano et al. (2018), respectively (Figures S3a, S3b). The peak location of the model of Nakata et al. (2019) was located ~10 km northwest of our models (Figure S3c), which was estimated by horizontally shifting the location of the slip distribution model from the teleseismic data estimated by JMA (shown later, in Section 5.2) to fit the coastal tide gauge waveforms. One reason for these differences may be the assumption of the fault geometry, but the more significant reason should be the station coverage and the source-station distance. The coastal tide gauges or the offshore stations used in these previous studies were located far from the source region and the stations at the offshore side of the source region were not used in these studies, whereas the S-net has better station coverage and a smaller source-station distance. This could provide a better constraint on the horizontal location and peak displacement amount to reproduce surprisingly well the tsunami waveforms not used for the inversion. Thanks to this improvement in the constraint, we believe that we can obtain a finite fault model with a higher resolution, as shown in the next section.

5 Fault modeling

5.1 Rectangular fault model with uniform slip

Here, we attempt to constrain the finite fault model of the off-Fukushima earthquake. The horizontal location and the peak subsidence of our tsunami source distribution are slightly different from the other previous models. Therefore, we first estimated the fault model based on a grid-search approach (Kubota et al., 2015; 2019). The procedure of the analysis is summarized in Text S2 but briefly explained here. We assume one planar rectangular fault with a uniform slip, with a set of unknown parameters (the fault model candidate). The unknown parameters are the fault location (longitude, latitude, and depth) and its dimensions (length L and width W). The strike, dip, and rake angles are fixed to the GCMT value (Table 1). The slip amount on fault D was adjusted to maximize the VR (Eq. (1)). The search range for the unknown parameters is summarized in Table S2, determined based on the tsunami source model. Using the fault model candidate, we calculated the seafloor displacement (Okada, 1992) and then calculated the pressure changes at each OBPG. This calculation procedure is identical to that for the Green's function of the tsunami source modeling (see Text S1). The goodness of each fault model candidate is evaluated by the VR values.

The horizontal location of the optimum fault is shown by dark red rectangle in Figure 4b. The detailed results are shown in Figure S4. We obtain the optimum fault model as L = 15 km, W = 10 km, and D = 467.7 cm ($M_0 = 2.1 \times 10^{19}$ Nm, M_w 6.8, assuming a rigidity of μ = 30 GPa). The center of this model is located at a depth of 6 km, ~10 km east of the GCMT centroid (Table 1). The GCMT centroid depth was 12 km and the aftershocks are mainly located at depths of ~ 20 km (Figures 1b and 1c), whereas the estimated fault is located at the very shallow part of the crust (Figure 1c and Table 1). This disagreement has also been pointed out by Gusman et al. (2017), who suggested that the aftershocks determined from the inland network are systematically deeper than the actual depth. The horizontal extent of the tsunami source is relatively narrow and is located at the northeast, compared with the tsunami source model (Figure S4a). The reproductivity of the S-net pressure waveforms is reasonable (Figure S4), although the VR is lower than that for the tsunami source modeling (VR = 59.3%). These mismatches are probably because of the simple assumption of the rectangular fault, which could not reproduce the southwest part of the tsunami source.

If we consider the empirical scaling relations from the magnitude, then the fault dimension is expected to be ~700 km^2 (e.g., Wells & Coppersmith, 1994). On the other hand, the estimated fault dimension of 150 km^2 is much smaller. In order to assess the dimensions of the rectangular fault, fixing the seismic moment M_0 and the fault center location to the optimum model and varying the fault dimensions, we simulate tsunamis and compare the waveforms of representative S-net stations near the focal area (Figure S5). If we assume a larger fault with L > 20 km, the arrival of the peak downheaval wave and its amplitude cannot be explained for the stations located northward (S2N01 and S2N02) or southward (S2N14 and S2N15) from the source. In addition, the sharp peak of the downheaval waves observed at the stations located eastward (S2N09, S2N10, S2N11, S2N12, and S2N15) from the source are not well reproduced by the fault width for the case in which W > 15 km. These results suggest that the fault dimensions should be $L \leq$ ~20 km and $W \leq$ ~15 km. Considering this range, the estimated fault dimensions are obviously smaller than expected based on the scaling relation. These much smaller fault dimensions are consistent with the size of the asperity, defined as the region of the large slip on the fault (e.g., Somerville et al., 1999), expected from the empirical relation deduced from the inland crustal earthquakes (Somerville et al., 1999; Miyakoshi et al., 2020). This may suggest that this optimum rectangular fault corresponds to the asperity.

5.2 Slip distribution

We then conduct a finite fault inversion to estimate the slip distribution (finite fault model). We assume a rectangular planar fault with dimensions of 45 km × 30 km, which passes through the optimum fault obtained by the grid search, and then the planar fault is divided into subfaults with size 3 km × 3 km. We then simulate the Green's function, (the pressure change waveforms excited by each subfault), using a similar calculation procedure to that explained above (see Texts S1 and S2). We estimated the slip amount of each subfault by the inversion scheme identical to the tsunami source modeling, but we imposed a nonnegativity constraint (Lawson & Hanson, 1974). The smoothing constraint was also imposed (Figure S6). The other details are described in Text S3.

The slip distribution obtained by the inversion analysis and the tsunami source distribution calculated from this slip distribution are shown in Figures 4a and 5a, respectively. The tsunami source distribution (Figure 5a) is similar to that obtained by the tsunami source inversion (Figure 3). The S-net and other tsunamis waveforms are explained (VR = 72.4%, Figures 5b–5g). We obtain a maximum slip of $D_{\max}$ = 637.2 cm, and the total seismic moment is $M_0 = 6.3 \times 10^{19}$ Nm (M_w 7.1, μ = 30 GPa). The large slip is concentrated in the northeastern part of the fault plane, corresponding to the rectangular fault estimated by the grid-search analysis. More specifically, subfaults with slip amounts with $D > 0.5 \times D_{\max}$ roughly correspond to the rectangular fault (subfaults marked by green lines in Figure 4a, 41% of the total M_0, M_w 6.9). In addition, a relatively small slip also extends to the southwestern part, which was not resolved in the grid-search analysis, probably because of the simple assumption of the uniform slip rectangular fault. If we take subfaults with slip amounts larger than $0.2 \times D_{\max}$, both large northeastern slip and relatively small southwestern slip are included (indicated by the thick black lines in Figure 4). Thus, we define these subfaults as the main rupture area. The main rupture area had dimensions of ~30 km × ~ 20 km, and 81% of the total moment was concentrated in the main rupture area. We calculate the centroid location $\mathbf{x}_c = (x_c, y_c, z_c)$ from the fault model, based on the slip-weighted average of subfault center locations over the main rupture area (pink star in Figure 4a, Table 1), defined as:

$$\mathbf{x}_c = \frac{\sum_i D_i \mathbf{x}_i}{\sum_i D_i}, \tag{2}$$

where the subscript i denotes the subfault index, $\mathbf{x}_i = (x_i, y_i, z_i)$ is the center location and D_i is the slip amount. We here used the subfaults within the main rupture area for the centroid calculation. The horizontal location of the centroid is located ~5 km southeast from the GCMT centroid.

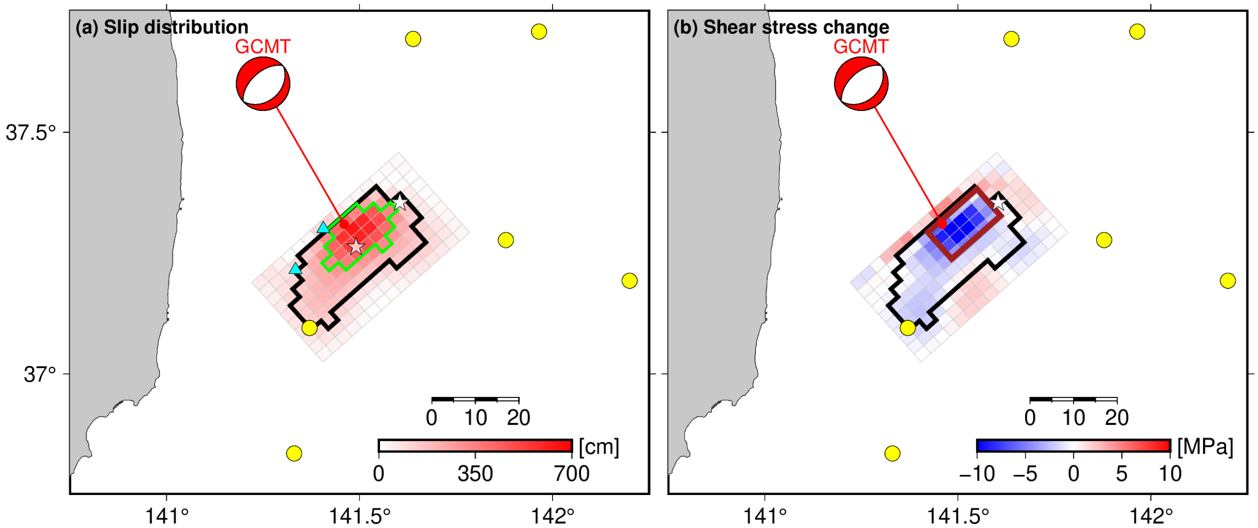

Figure 4. Result of the slip inversion. (a) Slip distribution (colored tiles). The pink and white stars indicate the slip-weighted averaged centroid and the JMA epicenter, respectively. Subfaults with slip amounts larger than $0.2 \times D_{\mathrm{max}}$ (the main rupture area) and larger than $0.5 \times D_{\mathrm{max}}$ are marked by thick black lines and green lines, respectively. (b) Shear stress change along the fault. Negative (blue) and positive (red) values denote the shear stress decrease (or positive stress drop) and increase (negative stress drop), respectively. The dark red rectangle denotes the optimum rectangular fault obtained by the grid-search analysis.

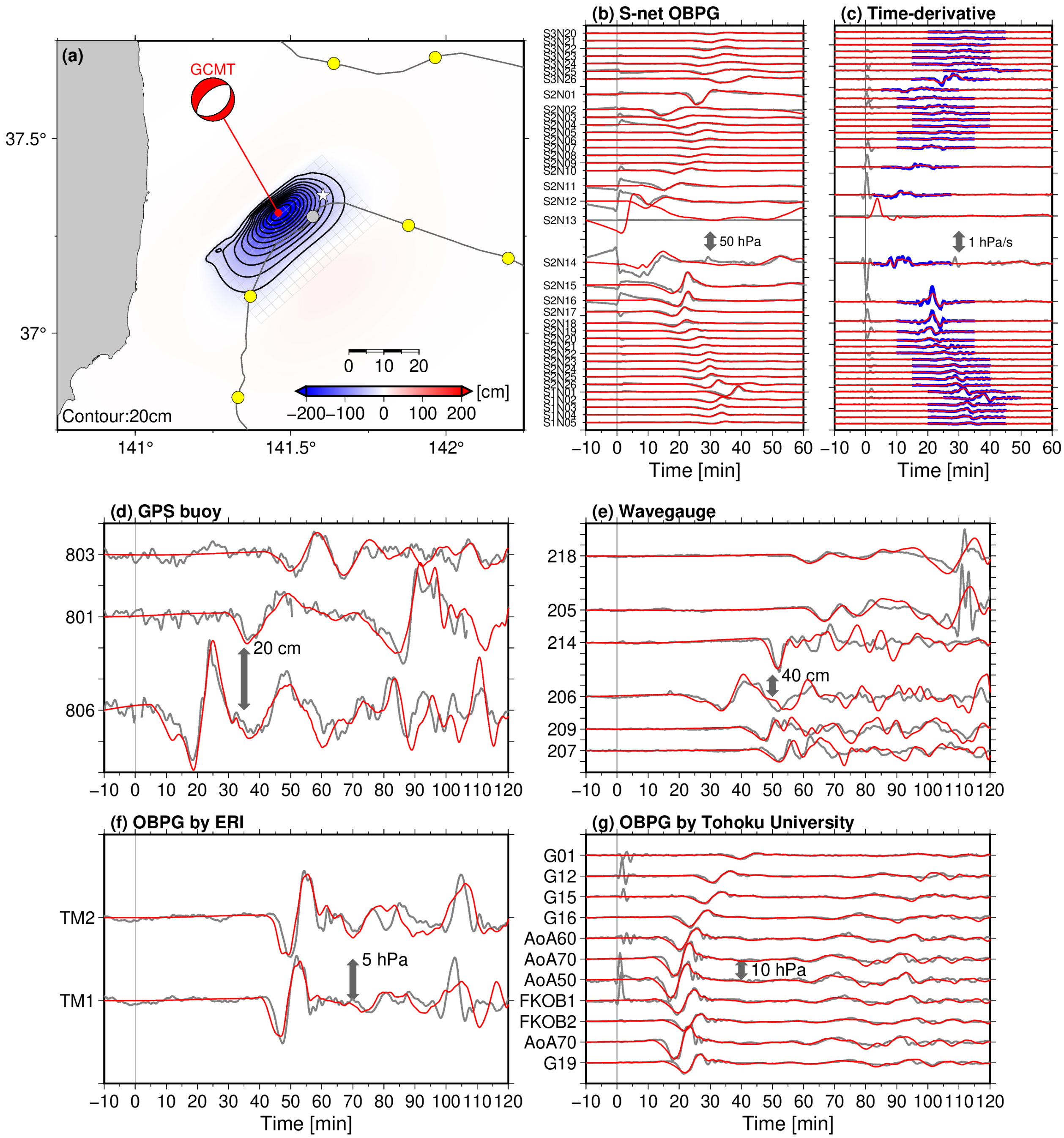

Figure 5. (a) Spatial distribution of the tsunami source calculated from the finite fault model. (b–g) Comparisons of the observed and simulated waveforms. See Figures 3 and 4 for the other detailed description.

We then evaluated the resolution of the slip dimension from the S-net data based on the recovery test (Figure S7). In the recovery test, we simulated pressure waveforms assuming the rectangular fault with slip amount of 100 cm and with various fault dimensions (3 km, 6 km, 9 km, 12 km, and 15 km). Then, these simulated waveforms are regarded as the observed data and inverted to estimate the slip distribution. The other conditions are identical to the original inversion. As a result, when assuming the smaller fault dimension (3 or 6 km), the estimated maximum slip was much smaller than the input and the recovered slip spreads out around the surroundings (Figure S7a–S7b). On the other hand, when assuming the faults with dimension of ≥ ~9 km, the slip smearing is small and the recovered maximum slip is consistent with the input amount (Figure S7c–S7f). This suggests that the resolution of the slip distribution is ~9 km.

We compare our fault model with the other models estimated using the teleseismic data and onshore geodetic data, by JMA and Geospatial Information Authority, Japan (GSI), respectively (Figure S8). The detailed fault parameters of these models are summarized in Table 1. The center of these fault models are ~10 km, almost consistent but slightly deeper compared with our model (~8 km). The location of the maximum slip in the JMA teleseismic fault model is almost identical to our model, although the maximum slip amount of 4.0 m was much smaller than ours (6.4 m) (Figure S8a). The fault length of the geodetic fault model by GSI was ~45 km, which was larger than the length of the main rupture area of our model (~30 km). The maximum slip of GSI model, 0.78 m, was much smaller than the average slip amount within the main rupture area of our model (2.8 m) (Figure S8b). This comparison possibly suggests the S-net data improved the spatial resolution of the slip distribution.

We then simulated the pressure waveforms for the representative S-net stations using the previously-proposed fault models (Adriano et al., 2018; Gusman et al., 2017; Nakata et al., 2019, Figure S9). We found the waveforms at the northern stations (~38°N) far from the focal area are reasonably reproduced by these model (Figures S9a) although the arrival times at the waveforms near the focal area (~36.5–37°N) and at the south (~36°N) were not reproduced (Figures S9b–S9c). The impulsive short-wavelength tsunami features at stations to the south direction (S2N15, S2N26, and S1N01) were not also explained well.

To investigate how the S-net data improved the resolution of the finite fault model, we then conducted the additional finite fault inversion using only the stations far from the focal area (Figures S10 and S11). The waveforms used for this additional inversion analysis is marked by blue traces in Figure S11c. The other settings is identical to the original analysis. As a result, the maximum slip of 3.8 m is almost similar to that obtained in the past studies (Figure S10a, S10c–S10e), but the large slip peak at the northeast part of the fault, around the rectangular fault estimated by the grid-search analysis (Section 5.1), was not resolved (Figure S10a). The waveforms for the far-field stations used for the inversion were reasonably explained, although the short-period impulsive tsunamis at the near-field S-net stations were not reproduced (Figure S11). In addition, we also conducted the recovery test to evaluate the resolution (Figure S12), with the identical procedure to that in the original analysis (Figure S7). We found that the recovered slip image was unsharp and the resolution was much lower than the original (> ~15 km). This result indicates the near-source S-net OBPGs are important to resolve the slip distribution and large slip component at the asperity with high resolution.

In our fault model, the downdip depth of the main rupture area was estimated as12.9–14.6 km. We evaluated the resolution of the downdip limit of the fault by additional tsunami simulations (Figure S13). We assume a simple rectangular fault with the length of 30 km and slip amount of 3 m, based on the main rupture area of the finite fault model (Figure S13a). We then vary the fault width so that the downdip limit of the fault is varied, and simulate tsunamis. As a result, the waveforms at the southern stations are different depending on the fault width, particularly for the stations located at the southeast from the epicenter (e.g., S2N18, S2N19, Figures S13c–S13d). At these stations, the simulated first down waves arrive earlier and its duration is longer, when the larger fault width are assumed (corresponding fault bottom depth is ≥ ~16 km), whereas the down waves are reproduced when the fault bottom end is assumed as 13–15 km. This suggests that the down dip end of the fault should be ≤ 15 km, consistent with the depth obtained in the finite fault modeling. However, the simulated waveforms are almost similar regardless of the fault width at the stations at the north (e.g., S3N26, S2N01, Figure S13b). Taking the point into account that the previous fault models (Figures S10c–S10e) were derived without using the stations located at the offshore side of the focal area, the use of the high-coverage S-net data, particularly located at the southeast of the focal area, potentially contributed to the constraint of the downdip depth of the fault of the off-Fukushima earthquake.

5.3 Stress drop

In Figure 4b, we calculate the distribution of the shear stress change along the fault (i.e., stress drop) by computing the shear stress change at the center of each subfault using the equation of Okada (1992). Here the shear stress change is calculated on fault plane along the slip vector (strike = 49°, dip = 36°, rake = −89°). The rectangular fault estimated by the grid-search analysis agrees well with the region where the shear stress is largely released (dark red rectangle in Figure 4b), indicating that the rectangular fault model corresponds to the asperity, as discussed above. We then calculate the energy-based stress drop, or the slip-weighted average stress drop, $\Delta\sigma_E$ (Noda et al., 2013) as:

$$\Delta\,\sigma_{\mathrm{E}} = \frac{\sum_i \; D_i \,\Delta\,\sigma_i}{\sum_i \; D_i}, \tag{3}$$

where D_i is the slip amount at the i-th subfault, and $\Delta\sigma_i$ is the stress drop at the i-th fault. Using the subfaults within the main rupture area ($D > 0.2 \times D_{\mathrm{max}}$), we obtain $\Delta\sigma_E = 4.2$ MPa. As it is a difficult issue to choose the appropriate area for the $\Delta\sigma_E$ calculation (Brown et al., 2015), we also calculate the stress drop using all subfaults and the subfaults with $D > 0.5 \times D_{\mathrm{max}}$ (the region marked by green lines in Figure 4a), and we obtain $\Delta\sigma_E = 3.3$ MPa and $\Delta\sigma_E = 6.8$ MPa, respectively. This value seems not so small as expected for the interplate earthquakes (~10^0 MPa, e.g., Kanamori & Anderson 1975), but rather is consistent with the intraplate earthquakes, which generally have larger stress drop values (e.g., Miyakoshi et al., 2020; Somerville et al., 1999).

In Figure S10b, we calculate the spatial distribution of the shear stress change from based on the fault model estimated by the additional inversion which uses only the far-field stations (Figure S10a). Using the subfaults within the area where the slip was larger than 20 % of the maximum slip, we obtain the average stress drop of $\Delta\sigma_E = 2.3$ MPa. However, because the S-net OBPGs near the source were not explained by this additional fault model (Figure S11), the actual average stress drop value should be larger than this value.

6. Discussion: implication for the intraplate stress regime

After the 2011 Tohoku earthquake, it has been reported that the normal-faulting seismicity significantly increased in the upper plate, which is thought to be related to the stress perturbation by the Tohoku earthquake (Figures 1d–1f, Asano et al., 2011; Hasegawa et al., 2012; Yoshida et al., 2012). This change in seismicity is interpreted as the result whereby the intraplate stress regime switched after the Tohoku earthquake from the horizontal compression to the horizontal extension (e.g., Hasegawa et al. 2012). As discussed previously, the use of the S-net tsunami data improved the constraint on the tsunami source and the fault model of the off-

Fukushima earthquake, which made it possible to obtain the detailed distribution of the shear stress reduction and the static stress drop. Using these results, we attempt to discuss the quantitative relationship between the crustal stress released during the off-Fukushima earthquake and the stress increase due to the 2011 Tohoku earthquake. This kind of discussion is typically difficult to conduct because it is rare that both the high-resolution fault model of the M~7 offshore earthquake and the significant stress perturbation due to the megathrust earthquake are available.

If the stress regime switched from the horizontal compression to the horizontal extension by the Tohoku earthquake around the off-Fukushima earthquake, the deviatoric stress, or the initial shear stress on the fault of the off-Fukushima earthquake, should be smaller than (or at least equivalent to) the static shear stress increase due to the Tohoku earthquake (Figure 6a). In other words, the stress drop of the off-Fukushima earthquake should be smaller than the shear stress increase due to the Tohoku earthquake. In Figure 7a, we calculate the shear stress change due to the Tohoku earthquake, using the fault model of Iinuma et al. (2012), along the fault geometry of the off-Fukushima earthquake. The shear stress change related to the Tohoku earthquake around the focal area of the off-Fukushima earthquake is only ~2 MPa, which is smaller than the stress drop of the off-Fukushima earthquake. We also calculated the shear stress change related to the Tohoku earthquake based on the fault model of Yamazaki et al. (2018), as ~1.1 MPa. In addition, at the some subfaults in which the large slip was estimated (e.g., the region marked by green lines in Figure 4a, $D > 0.5 \times D_{\mathrm{max}}$), the stress drop values are higher (> ~10 MPa, the slip-weighted average is $\Delta\sigma_{\mathrm{E}}$ = 6.8 MPa) and thus the stress discrepancy was much larger. The larger stress drop of the off-Fukushima earthquake than the stress increase after the Tohoku earthquake is inconsistent with the presumption that the intraplate stress regime switched by the stress change of the Tohoku earthquake. There may be other causes for the normal-faulting stress regime around the focal area, particularly at the asperity where the larger slip was estimated, of the off-Fukushima earthquake.

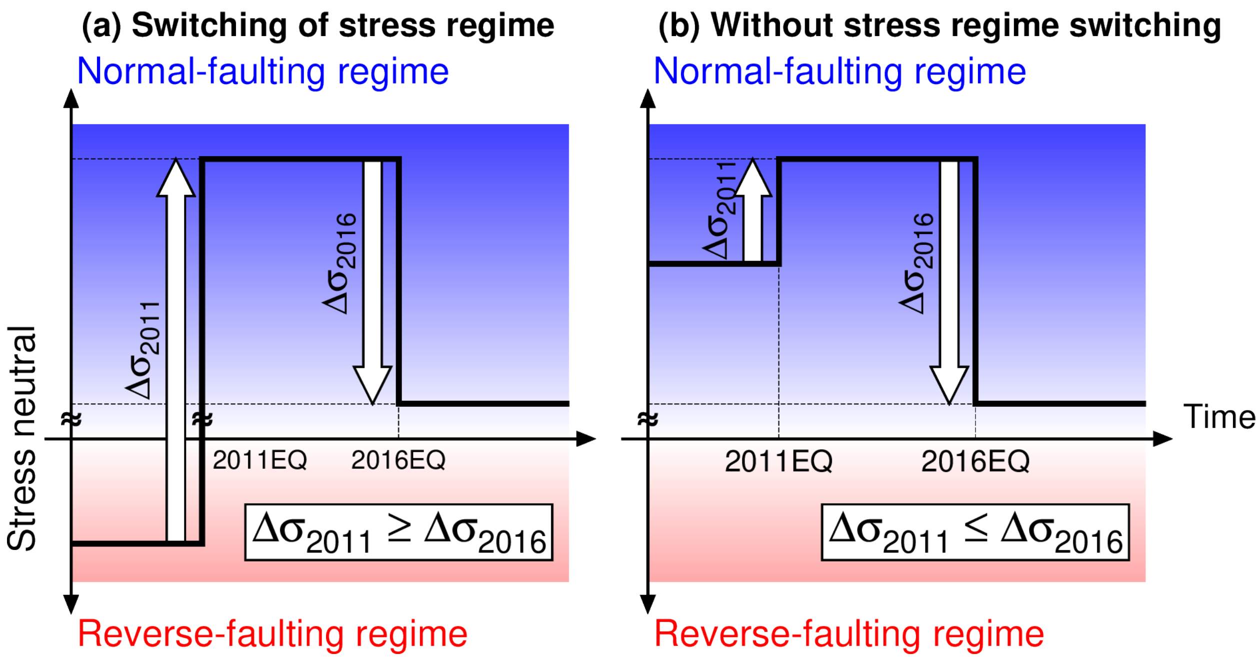

Figure 6. Schematic illustration of the temporal change of the stress regime around the off-Fukushima earthquake. The stress regimes (a) assuming the switching of the stress regime after the Tohoku earthquake and (b) without assuming the stress switching.

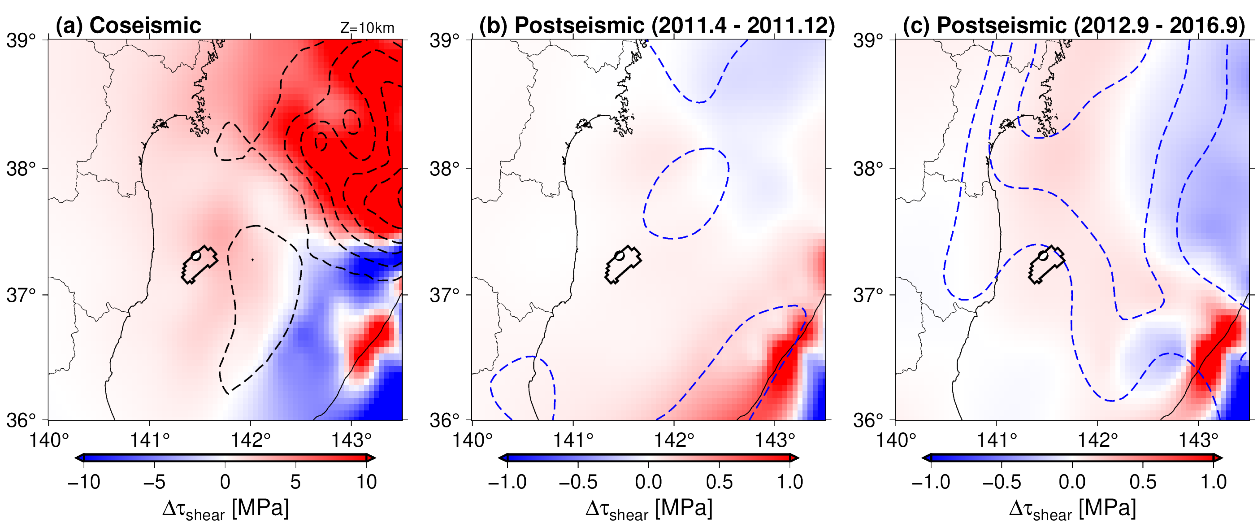

Figure 7. Horizontal distribution of the shear stress change on the 2016 off-Fukushima earthquake fault at a depth of 10 km. Shear stress changes along the fault geometry of the off-Fukushima earthquake due to (a) the Tohoku earthquake (Iinuma et al. 2012), (b) postseismic slip during April 2011 and December 2011 (Iinuma et al., 2016), and (c) Postseismic slip during September 2012 and September 2016 (Tomita et al. 2020). The main rupture area of the 2016

off-Fukushima earthquake inferred from the inversion analysis is also indicated by black lines. Note that the color scales are different in each subfigure.

One possible cause is the postseismic slip of the Tohoku earthquake (Iinuma et al., 2016; Tomita et al., 2020). After the Tohoku earthquake, the postseismic seafloor deformation was detected by the seafloor geodetic observation (Tomita et al., 2015; 2017), which was caused by the postseismic slip along the fault and the viscoelastic deformation (Iinuma et al., 2016; Sun et al., 2014; Tomita et al., 2020). Among the postseismic deformation, the afterslip along the plate interface is dominant in the south of the rupture area of the Tohoku earthquake, including the region off Fukushima, whereas the viscoelastic deformation dominates the northern part of the Tohoku earthquake rupture area (Iinuma et al., 2016; Tomita et al., 2020). We calculate the shear stress change on the 2016 fault geometry using the postseismic slip models to evaluate the contribution by the postseismic slip around the focal area. We calculate the stress change due to the postseismic slip models from 23 April 2011 to 10 December 2011 (Iinuma et al., 2016, Figure 7b) and during 2012 and 2016 (Tomita et al., 2020, Figure 7c), but the contributions by these postseismic slip models were minor (on the order of 10^{-1} MPa). We therefore concluded that the shear stress increase due to the postseismic slip could not resolve the apparent contradiction between the stress drop of the off-Fukushima earthquake and the shear stress increase after the Tohoku earthquake. This contradiction may arise from the assumption of the switching of the stress regime, which was a reverse-faulting and a normal-faulting regime before and after the Tohoku earthquake, respectively.

It will be reasonable to interpret this apparent contradiction that the horizontal extensional stress regime was already predominant around the 2016 off-Fukushima earthquake even before the Tohoku earthquake and the stress increase by the Tohoku earthquake further enhanced the extensional stress (Figure 6b), in contrary to the past studies which report the horizontal compressive stress attributed to the plate coupling force was widely dominant in Japan before the Tohoku earthquake (e.g., Terakawa & Matsu'ura, 2010; Wang & Suyehiro, 1999). In other words, the extensional stress accumulated even before the 2011 Tohoku earthquake was the dominant cause for the 2016 off-Fukushima earthquake. If we assume the stress state within the plate switched from the horizontal compression to the extension due to the stress change of a few MPa by Tohoku earthquake (Figure 6a), the 2016 earthquake must have occurred under the very low extensional stress level (less than a few MPa), but this is very unlikely to occur. Although there will be some uncertainties in the stress drop estimation of the 2016 earthquake and the stress increase due to the 2011 Tohoku earthquake, these uncertainties do not matter to this discussion and it is very reasonable to interpret that the stress state before the 2011 Tohoku earthquake was the horizontal extensional regime (Figure 6b). There are some recent reports that some normal-faulting microearthquakes occurred even before the Tohoku earthquake in the inland region of Fukushima prefecture (Imanishi et al., 2012; Yoshida et al., 2015a; 2015b), which supports our hypothesis of the normal-faulting stress regime being predominant in this location even before the Tohoku earthquake.

One possible reason for this normal-faulting stress regime is the effect of bending of the overriding plate, in which the horizontal extensional and compressional stresses develop at the shallower and the deeper portion of the plate, respectively (e.g., Fukahata & Matsu'ura, 2016; Hashimoto & Matsu'ura 2006; Turcotte & Schubert, 2002). Yoshida et al. (2015a) showed that the normal-faulting stress regime is dominant at depths shallower than ~15 km in this region, while the reverse-faulting stress regime is dominant at depths greater than ~15 km, which is consistent with the hypothesis. We can also consider the topographic effects (Sasajima et al., 2019; Wang et al., 2019) for the formation of the horizontal extensional stress. There may be another possible interpretation for this contradiction, that the stress regime switched to the reverse-faulting regime again by the off-Fukushima earthquake; However this is improbable because normal-faulting seismicity can be found nearby, even after one year from the earthquake (Figure 1f).

Some major normal-faulting earthquakes were reported around the focal area of the off-Fukushima earthquake in 1938 (Abe, 1977; Murotani, 2018). Furthermore, according to the geologic cross-section around the off-Iwaki gas field, located near the 2016 off-Fukushima earthquake, the northeast-southwest-trending reverse faults were developed at a depth shallower than 6 km, which are considered to have formed during Oligocene and Miocene (Iwata et al., 2002). Along this fault trace, it was also reported that the normal-faulting-type surface offsets with vertical offset of 5–10 m were found, and it was suggested that the direction of the tectonic stress flipped to the normal-faulting regime during Quaternary and normal-faulting earthquakes similar to the 2016 off-Fukushima earthquake repeatedly occurred along this fault (S. Toda, https://irides.tohoku.ac.jp/media/files/earthquake/eq/2016_fukushima_eq/20161122_fukushima_ eq_activefault_toda.pdf, in Japanese). These reports may support our hypothesis that the crustal stress regime was under the normal-faulting regime even before the Tohoku earthquake.

Note that the downdip limit of the main rupture area of our fault model the off-Fukushima earthquake is estimated as < ~15 km (Figure S9), which is approximately consistent with the downdip limit depth of the normal-faulting regime in the inland Fukushima region estimated by Yoshida et al. (2015a). This suggests that the horizontal extensional stress regime before the Tohoku earthquake around the focal area of the off-Fukushima earthquake is predominant at depths shallower than 15 km and the stress neutral zone related to bending of the overriding plate lies at a depth of ~15 km. However, we note that the normal-faulting seismicity extensively increased in the overriding plate after the Tohoku-Oki earthquake even at a depth deeper than 15 km (e.g., Asano et al., 2011; Hasegawa et al., 2012). This might suggest that the stress-neutral depth deepened around this region after the Tohoku earthquake.

As a summary of this discussion, the temporal change of the intraplate crustal stress around the off-Fukushima earthquake can be interpreted as follows. The horizontal extensional stress was predominant before the Tohoku earthquake within the shallowest part of the continental plate, but may not exceed the crustal strength. After the Tohoku earthquake, its stress perturbation enhanced the extensional stress, provoking the normal-faulting seismicity.

Before the 2011 Tohoku earthquake, no major seismicity was detected around the focal area of the off-Fukushima earthquake (e.g., Asano et al., 2011; Hasegawa et al., 2012) and the onshore seismic network could not detect micro-seismicity around this offshore region. On the other hand, the use of the S-net OBPGs could well constrain the fault modeling of the 2016 off-Fukushima earthquake, which provides an important implication for the crustal stress regime prior to the Tohoku earthquake, even though the S-net was not installed at that time. Such information about the stress regime is important to understand the spatio-temporal change of the intraplate stress state and the generation mechanisms of the intraplate earthquake, especially after a megathrust earthquake. Our analysis demonstrated that the analysis of the offshore S-net data provided implications for the crustal stress regime at the offshore region, which was difficult to discuss before the S-net was available. Although the S-net OBPG data contains the tsunami-irrelevant pressure change signals, careful analysis of this data significantly improves the constraint of the fault model and will deepen our understanding of the earthquake generation.

7 Conclusions

We examined the S-net tsunami data associated with the off-Fukushima earthquake on 21 November 2016 (M_w 7.1). We first processed the S-net OBPG data and found some pressure signals irrelevant to tsunami were observed: (1) an extremely large drift component and (2) an abrupt pressure step around the origin time. We discussed the cause of these tsunami-irrelevant signals and concluded that these signals were not due to the pressure sensors themselves but probably due to the observation system, although further investigations are necessary. We then analyzed the S-net data in order to estimate the tsunami source model and the fault model. Careful analysis of the S-net OBPG data provided the tsunami source distribution, which had a large subsidence with strike angle consistent with the GCMT solution. Our fault model suggested that the energy-based stress drop of the off-Fukushima earthquake is $\Delta\sigma_E$ ~4.2 MPa. The quantitative comparison between the stress drop and the static stress changes caused by the 2011 Tohoku earthquake and its postseismic slip suggested that the additional source of the horizontal extensional stress is necessary to explain the stress drop. We interpreted the stress regime around the off-Fukushima earthquake to be the horizontal extensional even before the Tohoku earthquake, related to the bending of the overriding plate. The S-net pressure data is very useful to constrain the tsunami source model and the finite fault model, even if the model is perturbed by the tsunami-irrelevant signals, which provided an important implication for the tectonic stress regime within the overriding plate.

Data Availability Statement

The S-net OBPG data (National Research Institute for Earth Science and Disaster Resilience [NIED], 2019, https://doi.org/10.17598/NIED.0007) are available with data request and permission, through the website of NIED (https://www.seafloor.bosai.go.jp, in Japanese). The data policy of the S-net data is shown in https://www.mowlas.bosai.go.jp/policy/?LANG=en. The NOWPHAS tsunami data is provided upon request to the Port and Airport Research Institute (PARI), in which the data redistribution is prohibited (the contact address is shown in https://nowphas.mlit.go.jp/pastdata/, in Japanese, accessed on 21 July, 2021). The data of the OBPGs installed by ERI of the University of Tokyo, as used in Gusman et al. (2017), are attached to this article as Supplementary Dataset S1, with permission of Masanao Shinohara, ERI. The OBPG data of Tohoku University are available in

Hino et al. (2021, https://doi.org/ 10.5281/zenodo.4961355). Station locations of the S-net OBPG are available at https://www.seafloor.bosai.go.jp/st_info/. The location of the OBPGs installed by the ERI is available in Gusman et al. (2017), as well as in Dataset S1. The locations of the NOWPHAS GPS buoys and wave gauges are available at https://nowphas.mlit.go.jp/pastdata/ (in Japanese). The locations of the OBPGs installed by Tohoku University are listed in Hino et al. (2021), as well as in Table S3.

We purchased the JTOPO30v2 bathymetry data from the Marine Information Research Center (http://www.mirc.jha.jp/en/) of the Japan Hydrographic Association. The plate boundary model in Figure 1 (Nakajima & Hasegawa, 2006) is available from the website of Fuyuki Hirose (https://www.mri-jma.go.jp/Dep/sei/fhirose/plate/PlateData.html, in Japanese, accessed on 21 July, 2021). The rotation data of the S-net sensor (Takagi et al., 2019) was provided by contacting Ryota Takagi, the lead author of Takagi et al. (2019). The slip models of the mainshock and postseismic slip of Iinuma et al. (2012; 2016) and Tomita et al. (2020) were provided by the corresponding authors of each article, Takeshi Iinuma and Fumiaki Tomita. The slip distribution models of Gusman et al. (2017), Adriano et al. (2018), and Nakata et al. (2019) are available in each paper. The finite fault model using the teleseismic data by JMA is shown in https://www.data.jma.go.jp/svd/eqev/data/sourceprocess/event/2016112205594689far.pdf (in Japanese, accessed on 21 July, 2021) and its digital data is available from https://www.data.jma.go.jp/svd/eqev/data/sourceprocess/data/2016112205594689far.zip (accessed on 21 July, 2021). The fault model using the onshore geodetic data by GSI is available from https://cais.gsi.go.jp/YOCHIREN/activity/214/214.e.html (accessed on 21 July, 2021) and https://cais.gsi.go.jp/YOCHIREN/activity/214/image214/008.pdf (in Japanese, accessed on 21 July 2021). The location of the seafloor bathymetry survey conducted by the Japan Agency for Marine-Earth Science and Technology [JAMSTEC] (blue triangles in Figure 4a) was taken from http://www.jamstec.go.jp/ceat/j/topics/20161208.html, http://www.jamstec.go.jp/j/about/press_release/20170301/ (in Japanese, accessed on 21 July, 2021).

The results of the tsunami source modeling (Figure 3) and the slip distribution (Figure 4) are available in the tgz compressed file, Dataset S2. The detailed description of the dataset is available in README file of the tgz file.

Acknowledgments

The present study was supported by JSPS KAKENHI Grant Number JP19K14818 and JP19H02409 from the Japan Society for the Promotion of Science. Discussions with Ryota Hino, Naoki Uchida, and Tatsuhiko Saito, about interpreting the S-net pressure signals and the results of the fault modeling, were fruitful. We would also like to thank Ryota Takagi, Takeshi Iinuma, and Fumiaki Tomita for providing their useful data. We thank the Editor Rachel Abercrombie and the Associate Editor, and two anonymous reviewers for their comments.

References

Abe, K. (1977). Tectonic implications of the large shioya-oki earthquakes of 1938. *Tectonophys*, *41*, 269–289. https://doi.org/10.1016/0040-1951(77)90136-6

Adriano, B., Fujii, Y., & Koshimura, S. (2018). Tsunami source and inundation features around Sendai Coast, Japan, due to the November 22, 2016 Mw 6.9 Fukushima earthquake. *Geoscience Letters*, *5*, 2. https://doi.org/10.1186/s40562-017-0100-9

Aoi, S., Suzuki, W., Chikasada, N. Y., Miyoshi, T., Arikawa, T., & Seki, K. (2019). Development and utilization of real-time tsunami inundation forecast system using s-net data. *Journal of Disaster Research*, *14*(2), 212–224. https://doi.org/10.20965/jdr.2019.p0212

Aoi, S., Asano, Y., Kunugi, T., Kimura, T., Uehira, K., Takahashi, N., & Ueda, H. (2020). MOWLAS : NIED observation network for earthquake , tsunami and volcano. *Earth, Planets and Space*, *72*, 126. https://doi.org/10.1186/s40623-020-01250-x

Asano, Y., Saito, T., Ito, Y., Shiomi, K., Hirose, H., Matsumoto, T., … Sekiguchi, S. (2011). Spatial distribution and focal mechanisms of aftershocks of the 2011 off the Pacific coast of Tohoku Earthquake. *Earth, Planets and Space*, *63*, 669–673. https://doi.org/10.5047/eps.2011.06.016

Baba, T., Hirata, K., Hori, T., & Sakaguchi, H. (2006). Offshore geodetic data conducive to the estimation of the afterslip distribution following the 2003 Tokachi-oki earthquake. *Earth and Planetary Science Letters*, *241*, 281–292. https://doi.org/10.1016/j.epsl.2005.10.019

Brown, L., Wang, K., & Sun, T. (2015). Static stress drop in the Mw 9 Tohoku-oki earthquake: Heterogeneous distribution and low average value. *Geophysical Research Letters*, *42*, 10,595–10,600. https://doi.org/10.1002/2015GL066361

Chadwick, W. W. J., Nooner, S. L., Zumberge, M. A., Embley, R. W., & Fox, C. G. (2006). Vertical deformation monitoring at Axial Seamount since its 1998 eruption using deep-sea pressure sensors. *Journal of Volcanology and Geothermal Research*, *150*, 313–327. https://doi.org/10.1016/j.jvolgeores.2005.07.006

Dhakal, Y. P., Kunugi, T., Suzuki, W., Kimura, T., Morikawa, N., & Aoi, S (2021). Strong motions on land and ocean bottom: Comparison of horizontal PGA, PGV, and 5% damped acceleration response spectra in northeast Japan and the Japan Trench area.

Bulletin of the Seismological Society of America, *111*. https://doi.org/10.1785/0120200368

Fukahata, Y., & Matsu'ura, M. (2016). Deformation of island-arc lithosphere due to steady plate subduction. *Geophysical Journal International*, *204*, 825–840. https://doi.org/10.1093/gji/ggv482

Fukuyama, E., Ishida, M., Dreger, D. S., & Kawai, H. (1998). Automated seismic moment tensor determination by using on-line broadband seismic waveforms. *Zisin 2*, *51*, 149–156 (in Japanese with English abstract). https://doi.org/10.4294/zisin1948.51.1_149

Gusman, A. R., Satake, K., Shinohara, M., Sakai, S., & Tanioka, Y. (2017). Fault slip distribution of the 2016 Fukushima earthquake estimated from tsunami waveforms. *Pure and Applied Geophysics*, *174*, 2925–2943. https://doi.org/10.1007/s00024-017-1590-2

Hardebeck, J. L., & Okada, T. (2018). Temporal stress changes caused by earthquakes: a review. *Journal of Geophysical Research: Solid Earth*, *123*, 1350–1365. https://doi.org/10.1002/2017JB014617

Hasegawa, A., Yoshida, K., Asano, Y., Okada, T., Iinuma, T., & Ito, Y. (2012). Change in stress field after the 2011 great Tohoku-Oki earthquake. *Earth and Planetary Science Letters*, *355–356*, 231–243. https://doi.org/10.1016/j.epsl.2012.08.042

Hashimoto, C., & Matsu'ura, M. (2006). 3-D simulation of tectonic loading at convergent plate boundary zones: Internal stress fields in northeast Japan. *Pure and Applied Geophysics*, *163*(9), 1803–1817. https://doi.org/10.1007/s00024-006-0098-y

Hino, R. (2015). An overview of the Mw 9, 11 March 2011, Tohoku earthquake. *Summary of the Bulletin of the International Seismological Centre*, *48*, 100–132. https://doi.org/10.5281/zenodo.998789

Hino, R., Suzuki, S., Sato, M., & Kubota, T. (2021) Ocean bottom pressure data of the 2016 Off-Fukushima earthquake obtained by Tohoku University [Data set]. Zenodo. http://doi.org/10.5281/zenodo.4961355

Hino, R., Inazu, D., Ohta, Y., Ito, Y., Suzuki, S., Iinuma, T., … Kaneda, Y. (2014). Was the 2011 Tohoku-Oki earthquake preceded by aseismic preslip? Examination of seafloor vertical deformation data near the epicenter. *Marine Geophysical Research*, *35*, 181–190. https://doi.org/10.1007/s11001-013-9208-2

Hua, Y., Zhao, D., Toyokuni, G., & Xu, Y. (2020). Tomography of the source zone of the great 2011 Tohoku earthquake. *Nature Communications*, *11*, 1163. https://doi.org/10.1038/s41467-020-14745-8

Iinuma, T., Hino, R., Kido, M., Inazu, D., Osada, Y., Ito, Y., … Miura, S. (2012). Coseismic slip distribution of the 2011 off the Pacific Coast of Tohoku Earthquake (M9.0) refined by means of seafloor geodetic data. *Journal of Geophysical Research*, *117*, B07409. https://doi.org/10.1029/2012JB009186

Iinuma, T., Hino, R., Uchida, N., Nakamura, W., Kido, M., Osada, Y., & Miura, S. (2016). Seafloor observations indicate spatial separation of coseismic and postseismic slips in the 2011 Tohoku earthquake. *Nature Communications*, *7*, 13506. https://doi.org/10.1038/ncomms13506

Imanishi, K., Ando, R., & Kuwahara, Y. (2012). Unusual shallow normal-faulting earthquake sequence in compressional northeast Japan activated after the 2011 off the Pacific coast of Tohoku earthquake. *Geophysical Research Letters*, *39*(9), L09306. https://doi.org/10.1029/2012GL051491

Inazu, D., & Hino, R. (2011). Temperature correction and usefulness of ocean bottom pressure data from cabled seafloor observatories around Japan for analyses of tsunamis, ocean tides, and low-frequency geophysical phenomena. *Earth, Planets and Space*, *63*(11), 1133–1149. https://doi.org/10.5047/eps.2011.07.014

Inoue, M., Tanioka, Y., & Yamanaka, Y. (2019). Method for near-real time estimation of Tsunami sources using ocean bottom pressure sensor network (S-net). *Geosciences*, *9*, 310. https://doi.org/10.3390/geosciences9070310

Iwata, T., Hirai, A., Inaba, T., & Hirano, M. (2002). Petroleum system in the Offshore Joban Basin, northeast Japan. *Journal of the Japanese Association for Petroleum Technology*, *67*(1), 62–71 (in Japanese with English abstract). https://doi.org/10.3720/japt.67.1_62

Kanamori, H., & Anderson, D. L. (1975). Theoretical basis of some empirical relations in seismology. *Bulletin of the Seismological Society of America*, *65*(5), 1073–1095.

Kanazawa, T., & Hasegawa, A. (1997). Ocean-bottom observatory for earthquakes and tsunami off Sanriku, north-eastern Japan using submarine cable. *Proceedings of International Workshop on Scientific Use of Submarine Cables*, 208–209.

Kanazawa, T., Uehira, K., Mochizuki, M., Shinbo, T., Fujimoto, H., Noguchi, S., et al. (2016). *S-net project, cabled observation network for earthquake and tsunamis* [Conference presentation]. Suboptic2016, Dubai. https://suboptic.org/wp-content/uploads/fromkevin/program/WE2B.3%20S-net%20Project,%20Cabled%20Observation%20Network%20for%20Earthquakes%20and%20Tsunamis.pdf

Kawaguchi, K., Sakuraba, S., Nagai, T., Nakai, K., Nukada, K., & Murase, H. (2017). Characteristics of observed low frequency wave profiles of the 2016 Fukushima-Off earthquake at offshore, shallow sea and coastal stations. *Journal of Japan Society of Civil Engineers, Ser. B3 (Ocean Engineering)*, *73*(2), I_743-I_748. https://doi.org/10.2208/jscejoe.73.I_743

Kodaira, S., Fujiwara, T., Fujie, G., Nakamura, Y., & Kanamatsu, T. (2020). Large coseismic slip to the trench during the 2011 Tohoku-Oki earthquake. *Annual Review of Earth and Planetary Sciences*, *48*, 321–343. https://doi.org/10.1146/annurev-earth-071719-055216

Kodaira, S., Iinuma, T., & Imai, K. (2021). Investigating a tsunamigenic megathrust earthquake in the Japan Trench. *Science*, *371*, eabe1169. https://doi.org/10.1126/science.abe1169

Kubota, T., Hino, R., Inazu, D., Ito, Y., & Iinuma, T. (2015). Complicated rupture process of the Mw 7.0 intraslab strike-slip earthquake in the Tohoku region on 10 July 2011 revealed by near-field pressure records. *Geophysical Research Letters*, *42*, 9733–9739. https://doi.org/10.1002/2015GL066101

Kubota, T., Saito, T., Ito, Y., Kaneko, Y., Wallace, L. M., Suzuki, S., Hino, R., & Henrys, S. (2018a). Using tsunami waves reflected at the coast to improve offshore earthquake source parameters: application to the 2016 Mw 7.1 Te Araroa earthquake, New Zealand. *Journal of Geophysical Research: Solid Earth*, *123*, 8767–8779. https://doi.org/10.1029/2018JB015832

Kubota, T., Suzuki, W., Nakamura, T., Chikasada, N. Y., Aoi, S., Takahashi, N., & Hino, R. (2018b). Tsunami source inversion using time-derivative waveform of offshore pressure records to reduce effects of non-tsunami components. *Geophysical Journal International*, *215*, 1200–1214. https://doi.org/10.1093/gji/ggy345

Kubota, T., Hino, R., Inazu, D., & Suzuki, S. (2019). Fault model of the 2012 doublet earthquake, near the up-dip end of the 2011 Tohoku-Oki earthquake , based on a near-field tsunami : implications for intraplate stress state. *Progress in Earth and Planetary Science*, *6*, 67. https://doi.org/10.1186/s40645-019-0313-y

Kubota, T., Saito, T., & Suzuki, W. (2020a). Millimeter-scale tsunami detected by a wide and dense observation array in the deep ocean: Fault modeling of an Mw 6.0 interplate earthquake off Sanriku, NE Japan. *Geophysical Research Letters*, *47*, e2019GL085842. https://doi.org/10.1029/2019GL085842

Kubota, T., Saito, T., Chikasada, N. Y., & Suzuki, W. (2020b). Ultrabroadband seismic and tsunami wave observation of high-sampling ocean-bottom pressure gauge covering periods from seconds to hours. *Earth and Space Science*, *7*, e2020EA001197. https://doi.org/10.1029/2020ea001197

Kubota, T., Saito, T., Chikasada, N. Y., & Sandanbata, O. (2021). Meteotsunami observed by the deep-ocean seafloor pressure gauge network off northeastern Japan. [Preprint]. *Earth and Space Science Open Archive*. https://doi.org/10.1002/essoar.10506159.1

Lay, T. (2018). A review of the rupture characteristics of the 2011 Tohoku-oki Mw 9.1 earthquake. *Tectonophysics*, *733*, 4–36. https://doi.org/10.1016/j.tecto.2017.09.022

Matsubara, M., Sato, H., Uehira, K., Mochizuki, M., Kanazawa, T., Takahashi, N., Suzuki, K., & Kamiya, S. (2019). Seismic velocity structure in and around the Japanese Island src derived from seismic tomography including NIED MOWLAS Hi-net and S-net data. In M. Kanao & G. Toyokuni (Eds.), *Seismic Waves - Probing Earth System*. IntechOpen. https://doi.org/10.5772/intechopen.86936.

Matsumoto, K., Takanezawa, T., & Ooe, M. (2000). Ocean tide models developed by assimilating TOPEX/POSEIDON altimeter data into hydrodynamical model: A global model and a regional model around Japan. *Journal of Oceanography*, *56*, 567–581. https://doi.org/10.1023/A:1011157212596

Miyakoshi, K., Somei, K., Yoshida, K., Kurahashi, S., Irikura, K., & Kamae, K. (2020). Scaling Relationships of Source Parameters of Inland Crustal Earthquakes in Tectonically Active Regions. *Pure and Applied Geophysics*, *177*, 1917–1929. https://doi.org/10.1007/s00024-019-02160-0

Mochizuki, M., Kanazawa, T., Uehira, K., Shimbo, T., Shiomi, K., Kunugi, T., et al. (2016). *S-net project: Construction of large scale seafloor observatory network for tsunamis and earthquakes in Japan* [Conference presentation]. AGU Fall Meeting 2016, American Geophysical Union, San Francisco.

Mulia, I. E., & Satake, K. (2021). Synthetic analysis of the efficacy of the S-net system in tsunami forecasting. *Earth, Planets and Space*, *73*, 36. https://doi.org/10.1186/s40623-021-01368-6

Murotani, S., Satake, K., & Fujii, Y. (2013). Scaling relations of seismic moment, rupture area, average slip, and asperity size for M~9 subduction-zone earthquakes. *Geophysical Research Letters*, *40*, 5070–5074. https://doi.org/10.1002/grl.50976

Murotani, S. (2018) Natural disasters that reached a milestone in Fukushima –The 1888 eruption of Bandai-san and the 1938 Fukushima-ken Toho-oki Earthquake– [Translated Title from Japanese]. *Earthquake Journal*, 66, 30–39 (in Japanese). Retrieved January 16, 2021, from https://www.adep.or.jp/public/img/66.pdf

Nagai, T. (1998). Development and improvement of the Japanese coastal wave observation network (NOWPHAS). *Journal of Japan Society of Civil Engineers*, *609*, 1–14. https://doi.org/10.2208/jscej.1998.609_1

Nakajima, J., & Hasegawa, A. (2006). Anomalous low-velocity zone and linear alignment of seismicity along it in the subducted Pacific slab beneath Kanto, Japan: Reactivation of subducted fracture zone? *Geophysical Research Letters*, *33*, L16309. https://doi.org/10.1029/2006GL026773

Nakata, K., Hayashi, Y., Tsushima, H., Fujita, K., Yoshida, Y., & Katsumata, A. (2019). Performance of uniform and heterogeneous slip distributions for the modeling of the November 2016 off Fukushima earthquake and tsunami, Japan. *Earth, Planets and Space*, *71*(1), 30. https://doi.org/10.1186/s40623-019-1010-1

National Research Institute for Earth Science and Disaster Resilience [NIED] (2019). NIED S-net [Data set]. https://doi.org/10.17598/nied.0007

Nishikawa, T., Matsuzawa, T., Ohta, K., Uchida, N., Nishimura, T., & Ide, S. (2019). The slow earthquake spectrum in the Japan Trench illuminated by the S-net seafloor observatories. *Science*, *365*, 808–813. https://doi.org/10.1126/science.aax5618

Noda, H., Lapusta, N., & Kanamori, H. (2013). Comparison of average stress drop measures for ruptures with heterogeneous stress change and implications for earthquake physics. *Geophysical Journal International*, *193*, 1691–1712. https://doi.org/10.1093/gji/ggt074

Polster, A., Fabian, M., & Villinger, H. (2009). Effective resolution and drift of paroscientific pressure sensors derived from long-term seafloor measurements. *Geochemistry, Geophysics, Geosystems*, *10*(8), Q08008. https://doi.org/10.1029/2009GC002532

Saito, T. (2019). *Tsunami generation and propagation*. Springer Japan, Tokyo. https://doi.org/10.1007/978-4-431-56850-6

Saito, T., Satake, K., & Furumura, T. (2010). Tsunami waveform inversion including dispersive waves: The 2004 earthquake off Kii Peninsula, Japan. *Journal of Geophysical Research*, *115*, B06303. https://doi.org/10.1029/2009JB006884

Saito, T., & Kubota, T. (2020). Tsunami modeling for the deep sea and inside focal areas. *Annual Review of Earth and Planetary Sciences*, *48*, 121–145. https://doi.org/10.1146/annurev-earth-071719-054845

Saito, T., Kubota, T., Chikasada, N. Y., Tanaka, Y., & Sandanbata, O. (2021). Meteorological tsunami generation due to sea-surface pressure change: Three-dimensional theory and synthetics of ocean-bottom pressure change [Preprint]. *Earth and Space Science Open Archive*. https://doi.org/10.1002/essoar.10504961.1

Sasajima, R., Shibazaki, B., Iwamori, H., Nishimura, T., & Nakai, Y. (2019). Mechanism of subsidence of the Northeast Japan forearc during the late period of a gigantic earthquake cycle. *Scientific Reports*, *9*, 5726. https://doi.org/10.1038/s41598-019-42169-y

Sawazaki, K., & Nakamura, T. (2020). "N"-shaped Y/X coda spectral ratio observed for in-line-type OBS networks; S-net and ETMC: interpretation based on natural vibration of pressure vessel. *Earth, Planets and Space*, *72*, 130. https://doi.org/10.1186/s40623-020-01255-6

Somerville, P., Irikura, K., Graves, R., Sawada, S., Wald, D., Abrahamson, N., Iwasaki, Y., Kagawa, T., Smith, N., & Kowada, A. (1999). Characterizing crustal earthquake slip models for the prediction of strong ground motion. *Seismological Research Letters*, *70*, 59–80. https://doi.org/10.1785/gssrl.70.1.59

Sun, T., Wang, K., Iinuma, T., Hino, R., He, J., Fujimoto, H., … Hu, Y. (2014). Prevalence of viscoelastic relaxation after the 2011 Tohoku-oki earthquake. *Nature*, *514*(7520), 84–87. https://doi.org/10.1038/nature13778

Suppasri, A., Leelawat, N., Latcharote, P., Roeber, V., Yamashita, K., Hayashi, A., … Imamura, F. (2017). The 2016 Fukushima earthquake and tsunami: Local tsunami behavior and recommendations for tsunami disaster risk reduction. *International Journal of Disaster Risk Reduction*, *21*, 323–330. https://doi.org/10.1016/j.ijdrr.2016.12.016

Takagi, R., Uchida, N., Nakayama, T., Azuma, R., Ishigami, A., Okada, T., … Shiomi, K. (2019). Estimation of the orientations of the S-net cabled ocean-bottom sensors. *Seismological Research Letters*, *90*, 2175–2187. https://doi.org/10.1785/0220190093

Takagi, R., Toyokuni, G., & Chikasada, N. (2020). Ambient noise correlation analysis of S-net records: extracting surface wave signals below instrument noise levels. *Geophysical Journal International*, *224*, 1640–1657. https://doi.org/10.1093/gji/ggaa548

Tanaka, M., Asano, K., Iwata, T., & Kubo, H. (2014). Source rupture process of the 2011 Fukushima-ken Hamadori earthquake: How did the two subparallel faults rupture? *Earth, Planets and Space*, *66*(1), 101. https://doi.org/10.1186/1880-5981-66-101

Tanaka, S., Matsuzawa, T., & Asano, Y. (2019). Shallow Low-Frequency Tremor in the Northern Japan Trench Subduction Zone. *Geophysical Research Letters*, *46*, 5217–5224. https://doi.org/10.1029/2019GL082817

Tanioka, Y. (2020). Improvement of Near-field Tsunami Forecasting Method Using Ocean Bottom Pressure Sensor Network (S-net). *Earth, Planets and Space*, *72*, 132. https://doi.org/10.1186/s40623-020-01268-1

Terakawa, T., & Matsu'ura, M. (2010). The 3-D tectonic stress fields in and around Japan inverted from centroid moment tensor data of seismic events. *Tectonics*, *29*, TC6008. https://doi.org/10.1029/2009TC002626

Toda, S., & Goto, H. (2016) https://irides.tohoku.ac.jp/media/files/earthquake/eq/2016_fukushima_eq/20161122_fukushima_eq_activefault_toda.pdf

Tomita, F., Kido, M., Osada, Y., Hino, R., Ohta, Y., & Iinuma, T. (2015). First measurement of the displacement rate of the Pacific Plate near the Japan Trench after the 2011

Tohoku-Oki earthquake using GPS/acoustic technique. *Geophysical Research Letters*, *42*(20), 8391–8397. https://doi.org/10.1002/2015GL065746

Tomita, F., Kido, M., Ohta, Y., Iinuma, T., & Hino, R. (2017). Along-trench variation in seafloor displacements after the 2011 Tohoku earthquake. *Science Advances*, *3*, e1700113. https://doi.org/10.1126/sciadv.1700113

Tomita, F., Iinuma, T., Ohta, Y., Hino, R., Kido, M., & Uchida, N. (2020). Improvement on spatial resolution of a coseismic slip distribution using postseismic geodetic data through a viscoelastic inversion. *Earth, Planets and Space*, *72*, 84. https://doi.org/10.1186/s40623-020-01207-0

Tsushima, H., Hino, R., Tanioka, Y., Imamura, F., & Fujimoto, H. (2012). Tsunami waveform inversion incorporating permanent seafloor deformation and its application to tsunami forecasting. *Journal of Geophysical Research*, *117*, B03311. https://doi.org/10.1029/2011JB008877

Tsushima, H., & Yamamoto, T. (2020). *Operational use of tsunami source inversion in near-field tsunami warning by JMA* [Conference presentation]. JpGU-AGU Joint Meeting 2020 Virtual, Online. https://confit.atlas.jp/guide/event/jpgu2020/subject/HDS08-12/advanced

Uchida, N., Nakajima, J., Wang, K., Takagi, R., Yoshida, K., Nakayama, T., … Asano, Y. (2020). Stagnant forearc mantle wedge inferred from mapping of shear-wave anisotropy using S-net seafloor seismometers. *Nature Communications*, *11*. https://doi.org/10.1038/s41467-020-19541-y

Uchida, N. & Bürgmann, R. (2021). A decade of lessons learned from the 2011 Tohoku-Oki earthquake. *Review of Geophysics*, *59*, e2020RG000713. https://doi.org/10.1029/020RG000713

Uehira, K., Kanazawa, T., Mochizuki, M., Fujimoto, H., Noguchi, S., Shinbo, T., et al. (2016). *Outline of seafloor observation network for earthquakes and tsunamis along the Japan Trench (S-net)* [Conference presentation]. EGU General Assembly 2016, European Geosciences Union, Vienna, Austria.

Wallace, L. M., Araki, E., Saffer, D., Wang, X., Roesner, A., Kopf, A., … Carr, S. (2016). Near-field observations of an offshore Mw 6.0 earthquake from an integrated seafloor and subseafloor monitoring network at the Nankai Trough, southwest Japan. *Journal of*

Geophysical Research: Solid Earth, *121*, 8338–8351. https://doi.org/10.1002/2016JB013417

Wells, D. L., & Coppersmith, K. J. (1994). New empirical relationships among magnitude, rupture length, rupture width, rupture area, and surface displacement. *Bulletin of the Seismological Society of America*, *84*(4), 974–1002.

Wang, K., & Suyehiro, K. (1999). How does plate coupling affect crustal stresses in Northeast and Southwest Japan? *Geophysical Research Letters*, *26*(15), 2307–2310. https://doi.org/10.1029/1999GL900528

Wang, K., Sun, T., Brown, L., Hino, R., Tomita, F., Kido, M., … Fujiwara, T. (2018). Learning from crustal deformation associated with the M9 2011 Tohoku-oki earthquake. *Geosphere*, *14*, 1–20. https://doi.org/10.1130/GES01531.1

Wang, K., Brown, L., Hu, Y., Yoshida, K., He, J., & Sun, T. (2019). Stable Forearc Stressed by a Weak Megathrust: Mechanical and Geodynamic Implications of Stress Changes Caused by the M = 9 Tohoku-Oki Earthquake. *Journal of Geophysical Research: Solid Earth*, *124*, 6179–6194. https://doi.org/10.1029/2018JB017043

Wang, Y., & Satake, K. (2021). Real-time tsunami data assimilation of S-net pressure gauge records during the 2016 Fukushima Earthquake. *Seismological Research Letters*. https://doi.org/10.1785/0220200447

Watts, D. R., & Kontoyiannis, H. (1990). Deep-ocean bottom pressure measurement: drift removal and performance. *Journal of Atmospheric and Oceanic Technology*, *7*, 296–306. https://doi.org/10.1175/1520-0426(1990)007<0296:DOBPMD>2.0.CO;2

Yamamoto, N., Aoi, S., Hirata, K., Suzuki, W., Kunugi, T., & Nakamura, H. (2016a). Multi-index method using offshore ocean-bottom pressure data for real-time tsunami forecast. *Earth, Planets and Space*, *68*, 128. https://doi.org/10.1186/s40623-016-0500-7

Yamamoto, N., Hirata, K., Aoi, S., Suzuki, W., Nakamura, H., & Kunugi, T. (2016b). Rapid estimation of tsunami source centroid location using a dense offshore observation network. *Geophysical Research Letters*, *43*, 4263–4269. https://doi.org/10.1002/2016GL068169

Yamazaki, Y., Cheung, K. F., & Lay, T. (2018). A self-consistent fault slip model for the 2011 Tohoku earthquake and tsunami. *Journal of Geophysical Research: Solid Earth*, *123*, 1435–1458. https://doi.org/10.1002/2017JB014749

Yoshida, K., Hasegawa, A., Okada, T., Iinuma, T., Ito, Y., & Asano, Y. (2012). Stress before and after the 2011 great Tohoku-oki earthquake and induced earthquakes in inland areas of eastern Japan. *Geophysical Research Letters*, *39*(3), L03302. https://doi.org/10.1029/2011GL049729

Yoshida, K., Hasegawa, A., & Okada, T. (2015a). Spatial variation of stress orientations in NE Japan revealed by dense seismic observations. *Tectonophysics*, *647*, 63–72. https://doi.org/10.1016/j.tecto.2015.02.013

Yoshida, K., Hasegawa, A., & Okada, T. (2015b). Spatially heterogeneous stress field in the source area of the 2011 Mw 6.6 Fukushima-Hamadori earthquake, NE Japan, probably caused by static stress change. *Geophysical Journal International*, *201*, 1062–1071. https://doi.org/10.1093/gji/ggv068

Yu, Z., & Zhao, D. (2020). Seismic evidence for water transportation in the forearc off northern Japan. *Journal of Geophysical Research: Solid Earth*, *125*, 2019JB018600. https://doi.org/10.1029/2019jb018600

Table 1. Fault parameters for the rectangular fault models.

Models	Fault center location			Strike [°]	Dip [°]	Rake [°]	M_0 [Nm]	Maximum vertical displacement [cm]	
	Longitude [°E]	Latitude [°N]	Depth [km][a]					Uplift	Subsidence
GCMT solution	141.46	37.31	12.0	49	36	−89	3.18×10^{19}	N/A	N/A
Tsunami source	N/A	N/A	N/A	N/A	N/A	N/A	N/A	16.3	238.4
Grid-search[ab]	141.5165	37.3105	6.0	49	36	−89	2.10×10^{19}	16.0	193.1
Slip distribution[a]	141.4908[c]	37.2630[c]	7.7[c]	49	36	−89	6.30×10^{19}	10.5	237.4
Gusman et al. (2017)	141.4532[c]	37.2705[c]	10.1[c]	45	41	−95	3.70×10^{19}	10.1	182.6
Adriano et al. (2018)	141.4406[c]	37.2695[c]	8.8[c]	49	35	−89	3.35×10^{19}	8.5	130.6
Nakata et al. (2019)	141.4660[c]	37.2932[c]	10.5[c]	50	48	Variable	8.52×10^{19}	29.7	222.2
JMA	141.5260[c]	37.2732[c]	10.5[c]	50	48	Variable	8.52×10^{19}	N/A	N/A
GSI	141.4971[d]	37.2821[d]	10.1[d]	47.6	63.2	−89.8	2.0×10^{19}	N/A	N/A

[a]Fault geometry is fixed to the GCMT value.

[b]Fault dimenson is L = 15 km, W = 10 km, and slip amount is D = 467.7 cm. The depths of the fault top and bottom are 3.1 km and 8.9 km, respectively.

[c]Slip-weighted average location is shown.

[d]Center of the rectangular fault is shown. The location of the left top corner is (141.28°E, 37.17°N, 2.2 km). The fault dimension and slip amount of the rectangular fault are L = 45.1 km and W = 17.7 km, D = 0.78 m. The top and bottom depths of the rectangular fault are 2.2 km and 18.0 km, respectively.

Journal of Geophysical Research: Solid Earth

Supporting Information for

Improving the constraint on the M_w 7.1 2016 off-Fukushima shallow normal-faulting earthquake with the high azimuthal coverage tsunami data from the S-net wide and dense network: Implication for the stress regime in the Tohoku overriding plate

Tatsuya Kubota[1], Hisahiko Kubo[1], Keisuke Yoshida[2], Naotaka Y. Chikasada[1], Wataru Suzuki[1], Takeshi Nakamura[3], and Hiroaki Tsushima[4]

[1] National Research Institute for Earth Science and Disaster Resilience, Japan.

[2] Graduate School of Science, Tohoku University, Japan.

[3] Central Research Institute of Electric Power Industry, Japan.

Contents of this file

Texts S1 to S3
Figures S1 to S13
Tables S1 to S3

Additional Supporting Information (Files uploaded separately)

Dataset S1 contains ocean-bottom pressure gauge data installed by Earthquake Research Institute, the University of Tokyo. Dataset S2 is the tgz compressed file which contain the results of the tsunami source modeling and the finite fault inversion.

Introduction

Texts S1, S2, and S3 explain the procedures for the tsunami source modeling, the grid-search analysis for the rectangular fault model, and the fault slip estimation, respectively. Figure S1 is the trade-off curve used to determine the weight of the smoothing constraint for tsunami source modeling. Figure S2 is the result of the tsunami source modeling using the pressure waveforms. Figure S3 compares the tsunami source expected from the previous studies. Figure S4 is the result of the grid-search analysis. Figure S5 evaluates the uncertainty of the fault dimension of the rectangular fault model. Figure S6 is the trade-off curve used to determine the weight of the smoothing constraint for the fault slip inversion. Figure S7 is the result of the recovery test. Comparison with the fault models deduced from the onshore data is shown Figure S8. Figure S9 shows the tsunami simulation from the previous fault models. Figures S10, S11 and S12 are the result of the finite fault inversion only using the stations far from the focal area. Figure S13 evaluates the downdip limit of the fault depth. The time windows used for the inversion analysis is summarized in Table S1. Table S2 shows the unknown parameters searched in the grid-search analysis. The station locations of the OBPGs installed by Tohoku University are listed in Table S3.

Text S1.

This text explains the procedure for the tsunami source modeling shown in Section 4. We first explain how to simulate the tsunami Green's function, which are the pressure change waveforms due to the tsunami and seafloor displacement at each OBPG caused by the displacement of the small region of seafloor. We distribute the small elements of the seafloor uplift (unit source elements) around the focal area (rectangular area in Figure 3a). The unit source element of the seafloor vertical displacement is given by

$$u_{ij}(x,y) = u_0 \left[\frac{1}{2} + \frac{1}{2}\cos\left(\frac{2\pi(x-x_i)}{L_x}\right)\right]\left[\frac{1}{2} + \frac{1}{2}\cos\left(\frac{2\pi(y-y_j)}{L_y}\right)\right]$$
$$\text{for} \quad x_i - \frac{L_x}{2} \le x \le x_i + \frac{L_x}{2},\ y_j - \frac{L_y}{2} \le y \le y_j + \frac{L_y}{2}, \tag{S1}$$

which takes the maximum value of $u_0 = 1$ cm at (x_i, y_j). Here, L_x and L_y are the spatial extent of the unit source element along the *x*- and *y*-directions, respectively. We assume that $L_x = L_y = 4$ km. Each of the unit sources overlaps with adjacent unit sources with a horizontal interval of $\Delta L_x = L_x/2$ and $\Delta L_y = L_y/2$. The numbers of unit sources along the *x*-direction and *y*-directions are $N_x = 25$ and $N_y = 25$, respectively, and the total number of unit sources is $N = N_x \times N_y = 625$. The size of the analytical area where the unit sources are distributed is 50 km × 50 km.

Using the seafloor vertical displacement from the unit sources, we calculate tsunamis using the following procedure. We assume the initial sea-surface height change assuming that the sea-surface displacement is equal to the seafloor displacement. We then solve the linear dispersive tsunami equation (Saito et al., 2010; Saito, 2019) in Cartesian coordinates with the staggered grid in order to simulate tsunamis:

$$\begin{gathered}
\frac{\partial M}{\partial t} + g_0 h \frac{\partial \eta}{\partial x} = \frac{1}{3} h^2 \frac{\partial^2}{\partial x \partial t}\left(\frac{\partial M}{\partial x} + \frac{\partial N}{\partial y}\right) \\
\frac{\partial N}{\partial t} + g_0 h \frac{\partial \eta}{\partial y} = \frac{1}{3} h^2 \frac{\partial^2}{\partial y \partial t}\left(\frac{\partial M}{\partial x} + \frac{\partial N}{\partial y}\right), \\
\frac{\partial \eta}{\partial t} = -\frac{\partial M}{\partial x} - \frac{\partial N}{\partial y}
\end{gathered} \tag{S2}$$

where the variable η is the sea surface height anomaly (tsunami height), *M* and *N* are the velocity components integrated along the vertical direction over the seawater depth, *h* is the water depth, and g_0 =9.8 m/s^2 is the gravitational constant. For water depth *h*, we use the JTOPO30 data with a spatial resolution of 30 arcsec, provided by the Marine Information Research Center of the Japan Hydrographic Association (http://www.mirc.jha.jp/en/), interpolating the spatial interval of $\Delta x = \Delta y = 1$ km. We assume that the displacement occurs instantaneously, at time $t = 0$ s. The temporal interval of the calculation is $\Delta t = 1$ s. After the calculation, we calculate the pressure change *p* at each OBPG location by subtracting the pressure offset change due to the seafloor displacement from the simulated sea-surface height change (Tsushima et al., 2012):

$$p = \rho_0 g_0 (\eta - u_z), \tag{S3}$$

where ρ_0 is the density of seawater. Here we suppose seawater density ρ_0 ~1.02 g/cm^3 and g_0 =9.8 m/s^2, so that a seawater column height change of 1 cm H_2O can be approximated as a pressure change of 1 hPa (i.e., $\rho_0 g_0 = 1$ hPa/cm). We finally apply the same bandpass filter to the simulated waveform as that applied to the observation.

In order to estimate the tsunami source, we use the time-derivative waveforms of the bandpass-filtered pressure waveforms for the inversion analysis ($\partial p/\partial t$, Figure 3c), because the time-derivative of the step signal becomes the impulse signal and thus does not contain the offset change, which can reduce the artificials due to the tsunami-irrelevant steps (Kubota et al., 2018b). The data time window used for the modeling, which includes the main part of the tsunami (indicated by the blue traces in Figure 3c), is manually determined. We solve the following observation equation:

$$\begin{pmatrix} \mathbf{d} \\ \mathbf{0} \end{pmatrix} = \begin{pmatrix} \mathbf{H} \\ \alpha \mathbf{S} \end{pmatrix} \mathbf{m} \tag{S4}$$

The data vector $\mathbf{d}$ consists of the time-derivative waveforms of the observed pressure $\partial p/\partial t$, and the matrix $\mathbf{H}$ consists of the time-derivative of the tsunami Green's functions. The vector **m** consists of the amounts of the displacement of the unit sources, which are the unknown parameters to be solved. The matrix **S** indicates the constraint for the spatial smoothing (e.g., Baba et al., 2006) and the parameter α is its weight. The goodness of the estimated source is evaluated using the variance reduction (VR):

$$\mathrm{VR} = \left(1 - \frac{\sum_i \left(d_i^{\mathrm{obs}} - d_i^{\mathrm{cal}}\right)^2}{\sum_i \ {d_i^{\mathrm{obs}}}^2}\right) \times 100\ (\%) \tag{S5}$$

where d_i^{obs} and d_i^{cal} are the *i*-th data of the observed and calculated time-derivative pressure waveforms, respectively. The smoothing weight α is determined based on the trade-off between the weight and the VR (Figure S1) in order to avoid both the overfitting and oversmoothing of data.

Text S2.

This text explains the procedure for the grid-search analysis to estimate the planar rectangular fault model, shown in Section 5.1. The modeling procedure is mostly based on the approach proposed by Kubota et al. (2015; 2019). In the grid-search, we assume one planar rectangular fault with a uniform slip. The strike angle of the fault is fixed to the GCMT value (strike = 49°), considering the consistency with the direction of the northeast-southwest extent of the tsunami source. Since the dip and rake angles cannot be constrained only from the tsunami source, we assume these angles based on the GCMT solution (dip = 35° and rake = −89°), as inferred from the analysis of the teleseismic data. To find the optimum model that best reproduces the S-net waveforms, we vary the other fault parameters and simulate tsunamis. The unknown parameters of the rectangular fault that we search are the fault center location (longitude, latitude, and depth) and its dimensions (length *L* and width *W*). The slip amount on fault *D* is adjusted to maximize the VR in Eq. (S5). The search range for these parameters is summarized in Table S2, which is determined based on the tsunami source model obtained in the previous section. Using an assumed rectangular fault with a set of parameters (the fault model candidate), we calculated the seafloor displacement (Okada, 1992). Then, using the seafloor displacemet as the initial sea surface height, we simulated tsunamis with the same simulation scheme as the calculation of the Green's function for the tsunami source inversion (Text S1). After the calculation, we calculate the pressure changes at the OBPG stations using Eq. (S3). Finally we evaluate the goodness of each of the fault model candidates is evaluated using the VR values (Eq. (S5)), using the same time window as used in the inversion analysis (blue traces in Figure S4, Table S1).

Text S3.

This text describes the procedure of the finite fault slip inversion, shown in Section 5.2. The modeling procedure is almost similar to that reported by Kubota et al. (2018a). We first assume a rectangular planar fault with dimensions of 45 km × 30 km, which is supposed to pass through the optimum fault obtained by the grid search (Text S2). Then, this planar fault is divided into small rectangular subfaults with size of 3 km × 3 km. We then simulate the Green's function (i.e., the pressure change waveforms excited by each subfault) using a similar calculation procedure to that used in the grid-search analysis. The seafloor vertical displacements are calculated from each subfault using the equations of Okada (1992), assuming a unit slip of 1 m. In this calculation, the strike, dip, and rake angles are fixed to the GCMT value, as adopted in the finite fault inversion. Then tsunami is calculated using the vertical displacement distribution as the initial sea surface height change (Eq. (S2)). After the calculation, the pressure change is calculated by subtracting the component of the seafloor vertical deformation from the simulated sea surface height change (Eq. (S3)), to obtain the Green's function for the finite fault slip inversion.

Using the Green's function for the finite fault slip inversion, simulated by the procedure shown above, we solve the following observation equation, which is similar to the tsunami source inversion:

$$\begin{pmatrix} \mathbf{d} \\ \mathbf{0} \end{pmatrix} = \begin{pmatrix} \mathbf{G} \\ \alpha\mathbf{S} \end{pmatrix} \mathbf{m}. \tag{S6}$$

The data vector $\mathbf{d}$ consists of the time-derivative waveforms of the observed pressure $\partial p/\partial t$, and the matrix $\mathbf{G}$ consists of the time-derivative of the Green's functions for the finite fault slip inversion. The vector **m** consists of the fault slip amount for each subfault (unit: [m]), which are the unknown parameters to be solved. The matrix **S** indicates the constraint for the spatial smoothing (e.g., Baba et al., 2006) and the parameter α is its weight.

When solving this observation equation, we imposed a nonnegativity constraint (Lawson & Hanson, 1974) because the negative slip (i.e., reverse-faulting slip component) is quite unlikely to occur. The weighting of the smoothing constraint α is determined based on the trade-off curve between its weight and VR value (Figure S6).

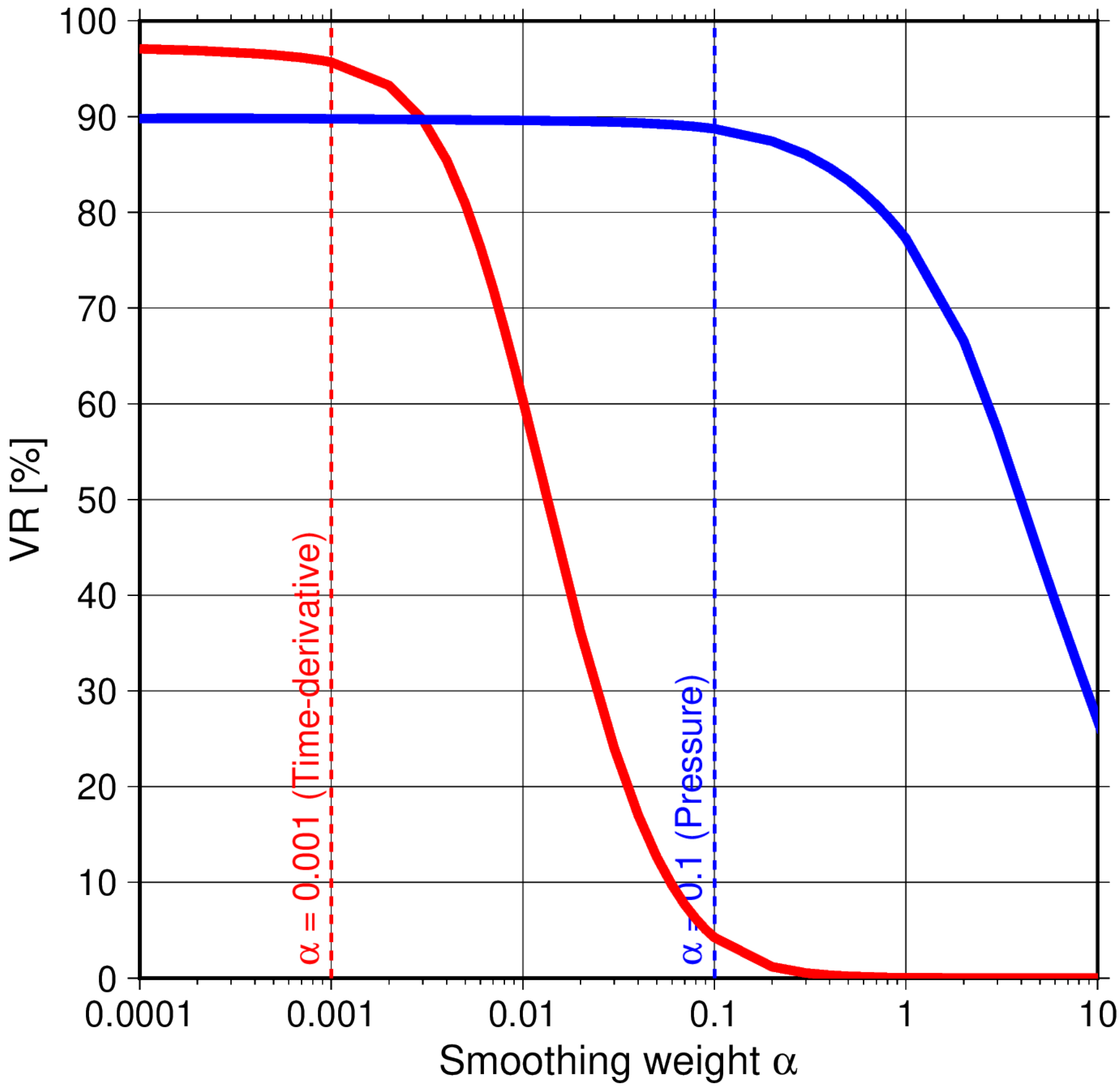

Figure S1. Trade-off curve between the smoothing weight α and VR. Red and blue solid lines are the trade-off curves for the inversions using the time-derivative waveform of the pressure (Figure 4) and the pressure waveform (Figure S2), respectively. Dashed lines denote the weight values used for the inversion analyses. Note that the VR values are calculated by using the time-derivative pressure waveforms for the inversion using the time derivative-waveforms (red), and by using the pressure waveforms for the inversion using the pressure waveforms (blue), respectively.

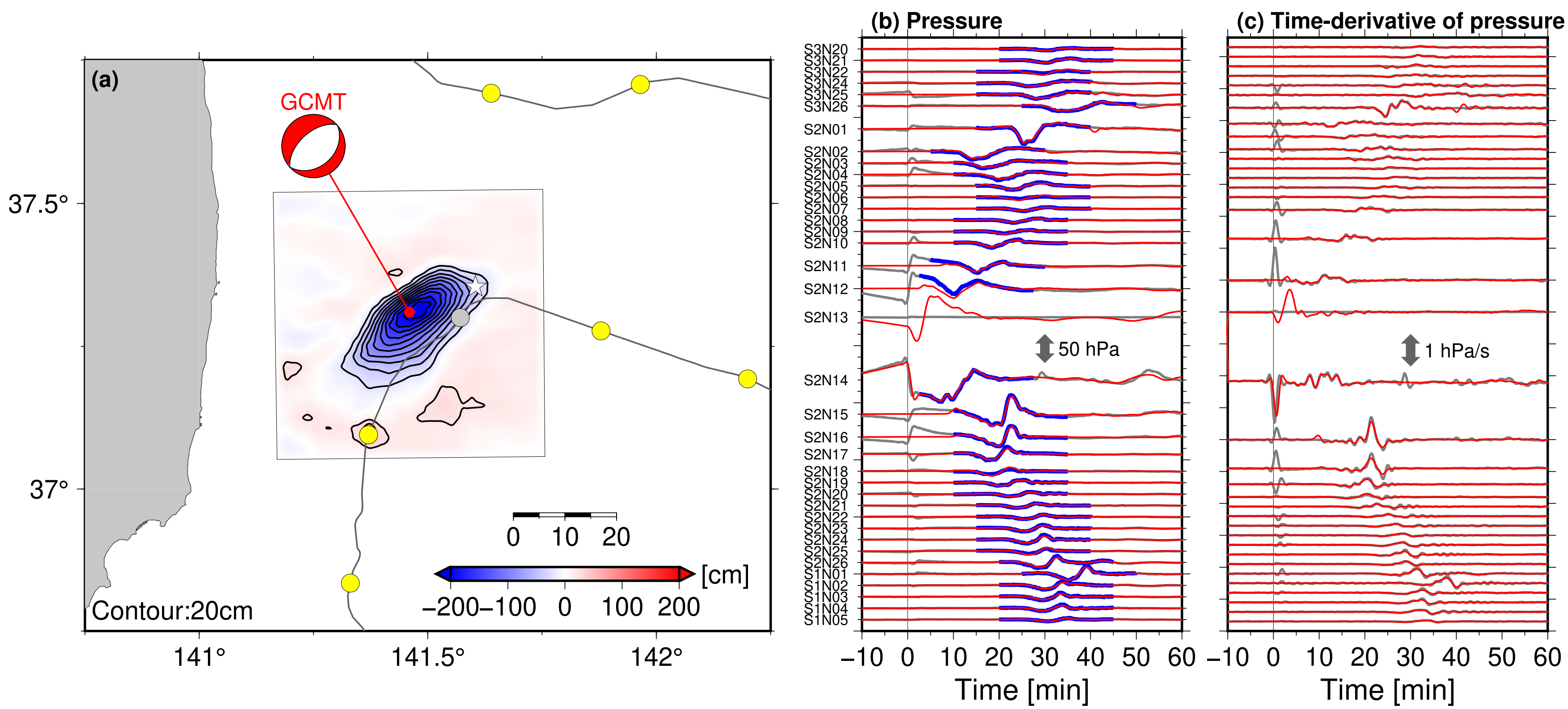

Figure S2. Results of the tsunami source inversion based on the conventional method. (a) Spatial distribution of the tsunami source. Contour lines denote the subsided region with intervals of 20 cm. The white star is the JMA epicenter. The yellow and gray circles show the S-net OBPGs used or not used, respectively, for inversion analysis. Comparisons of (b) the pressure waveforms and (c) the time-derivative waveforms. The gray and red traces denote the observed waveforms and simulated waveforms from the tsunami source model. Traces marked by blue lines denote the time window used for the inversion analysis.

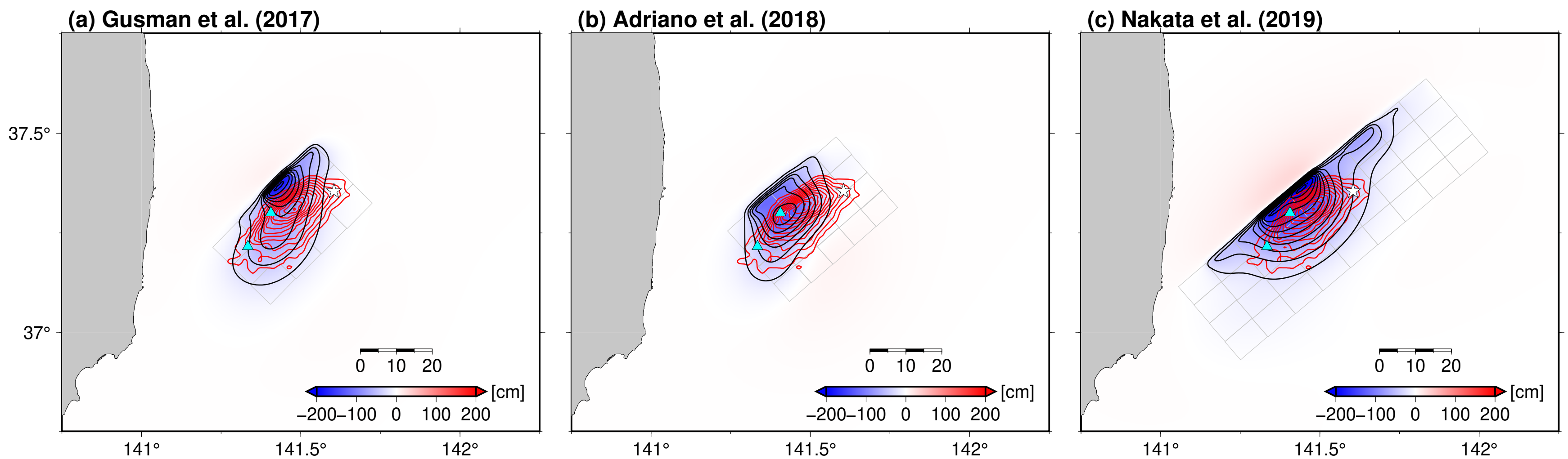

Figure S3. Comparison of the tsunami source calculated from the finite fault models of the previous studies (black contours) and the tsunami source model (red). Models of (a) Gusman et al. (2017), (b) Adriano et al. (2018), and (c) Nakata et al. (2019) are shown. The contour intervals are 20 cm. The configuration of the fault is also shown by gray lines.

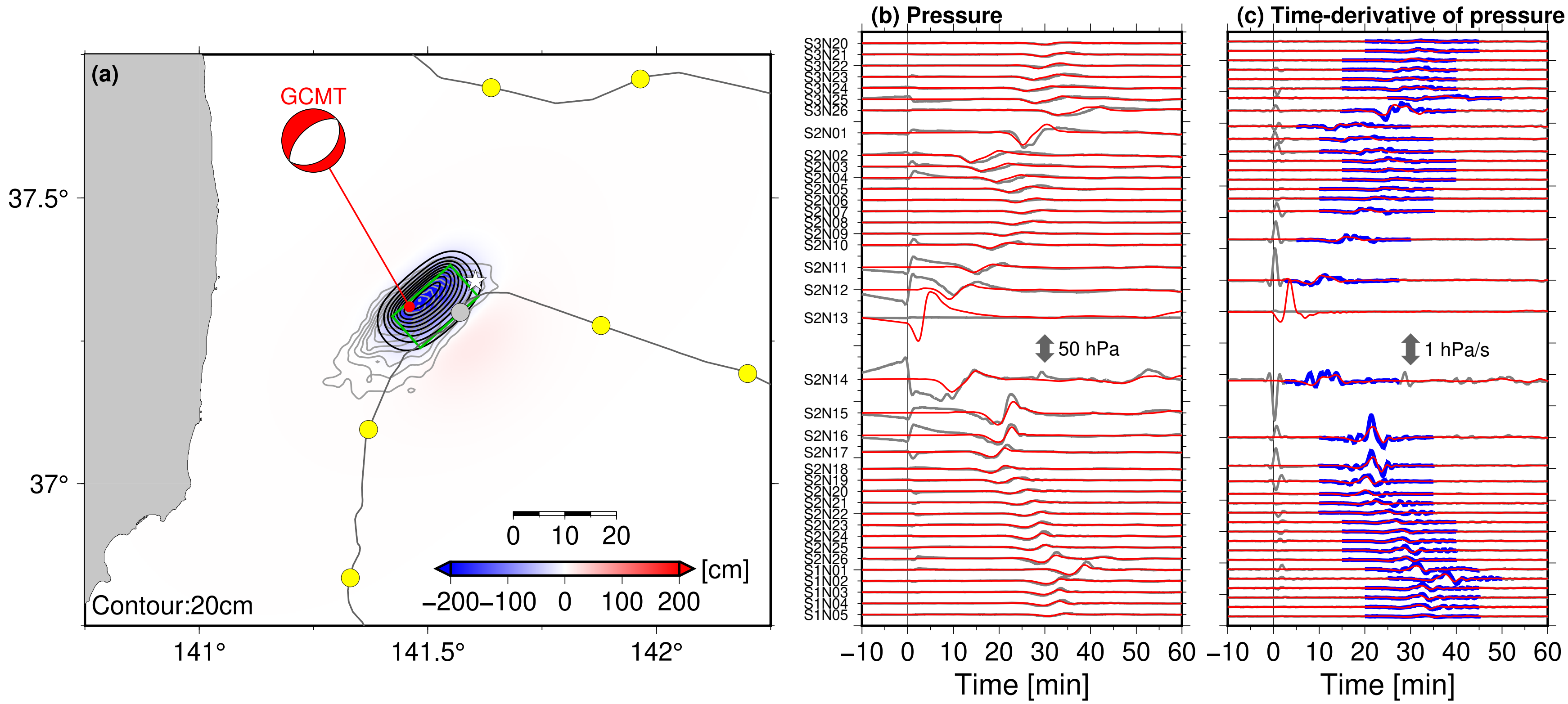

Figure S4. Results of the grid-search analysis. (a) Spatial distribution of the tsunami source. The green rectangle shows the location of the rectangular fault model. Black contours are the tsunami source calculated from the rectangular fault model (Table 1). The distribution of the tsunami source model obtained by the inversion is also shown by gray contours. Comparisons of (b) the pressure waveforms and (c) the time-derivative waveforms. See Figure 3 and S2 for a detailed explanation of the figure.

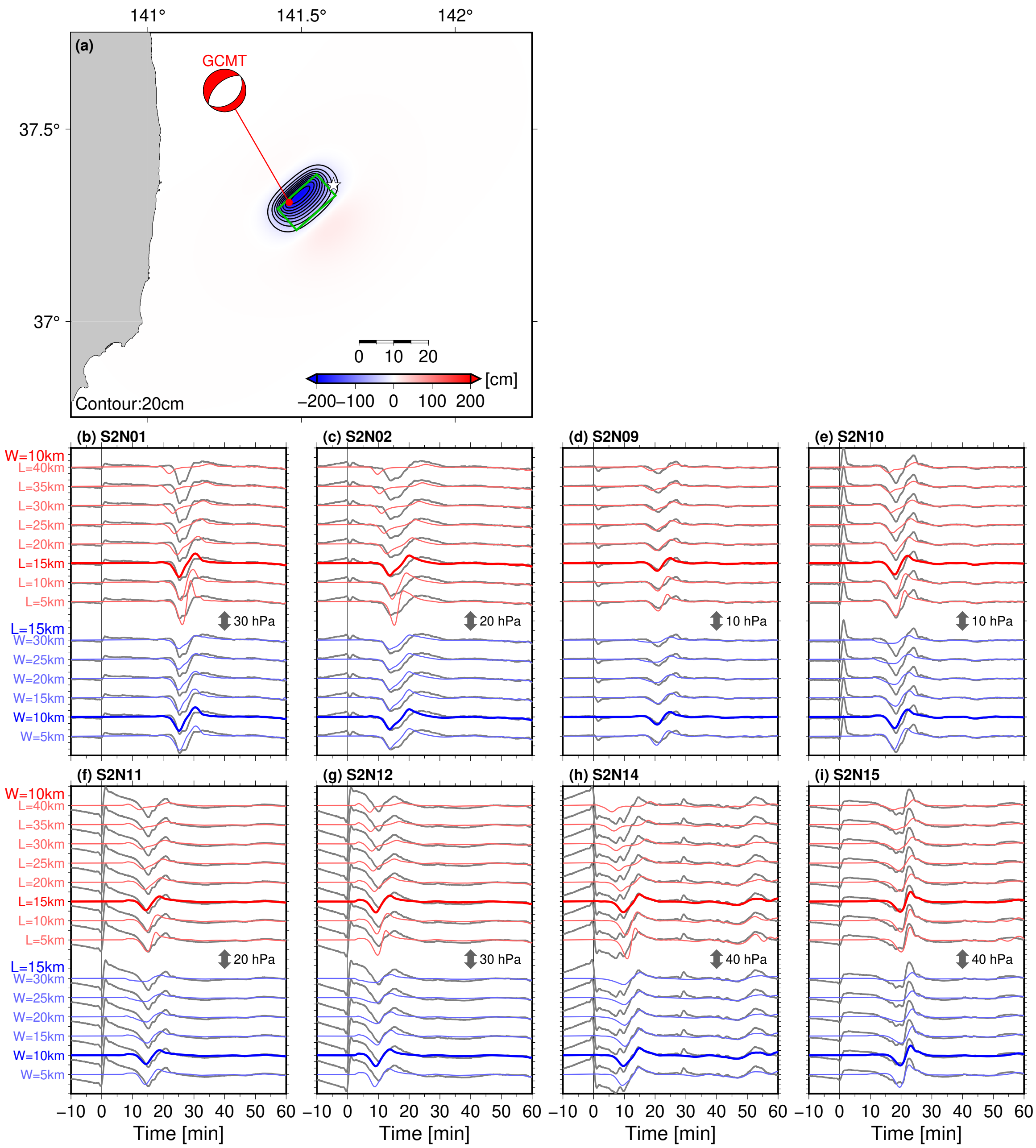

Figure S5. (a) Horizontal location of the optimum rectangular fault model. The green rectangle shows the location of the rectangular fault model and countour lines are the distribution of the tsunami source calculated from the rectangular fault model. (b–i) Evaluation of the fault dimension. Comparisons of the stations near the epicenter between the observed (gray) waveform and the simulated waveforms from the varied fault dimensions are shown. The simulated waveforms with thick red and blue traces denote the optimum rectangular fault.

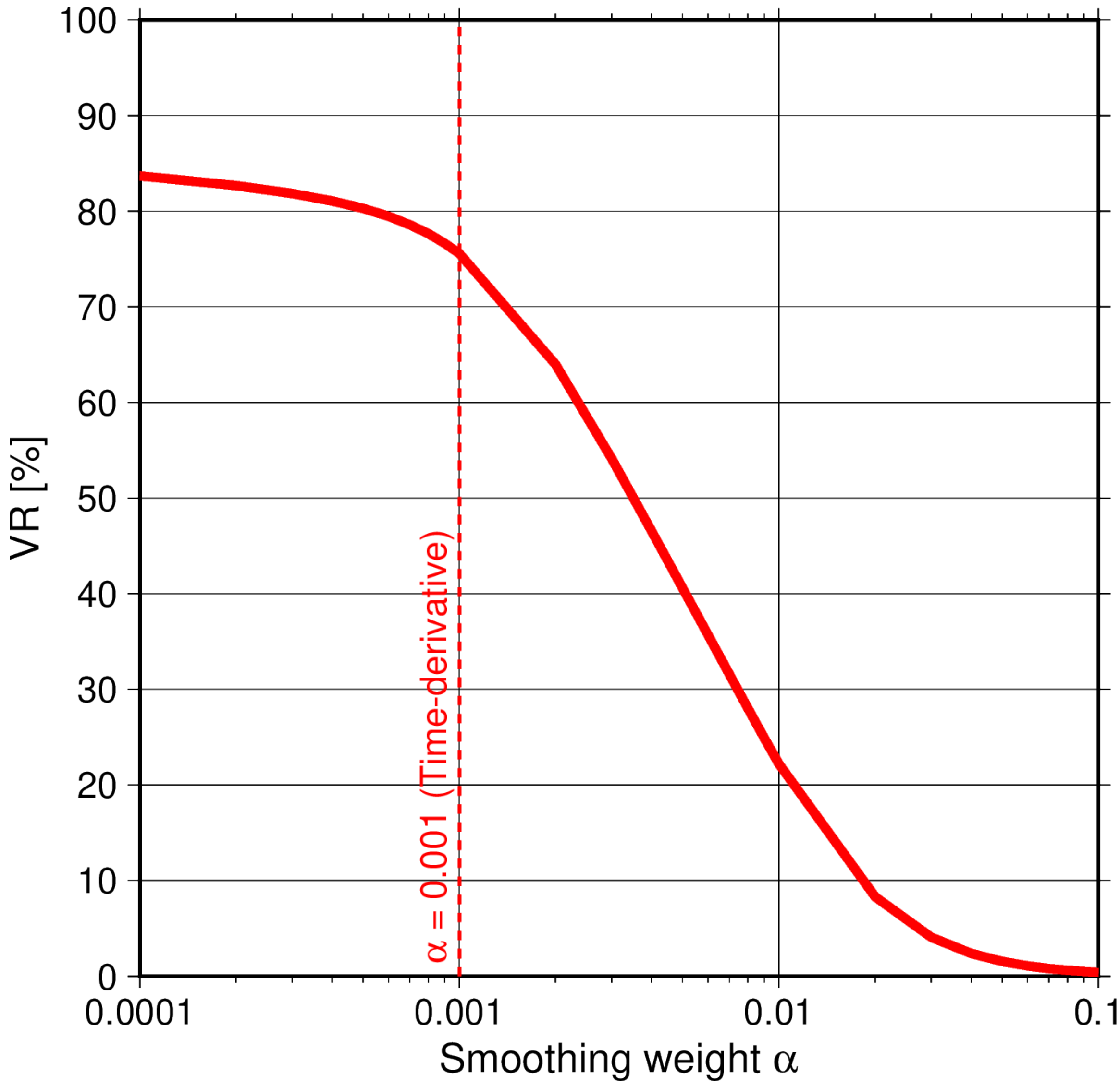

Figure S6. Trade-off curve between the smoothing weight α and VR for the finite fault slip inversion. Red solid line is the trade-off curves for the inversions using the time-derivative waveform of the pressure (Figure 4). Dashed lines denote the weight values adopted for the inversion analyses.

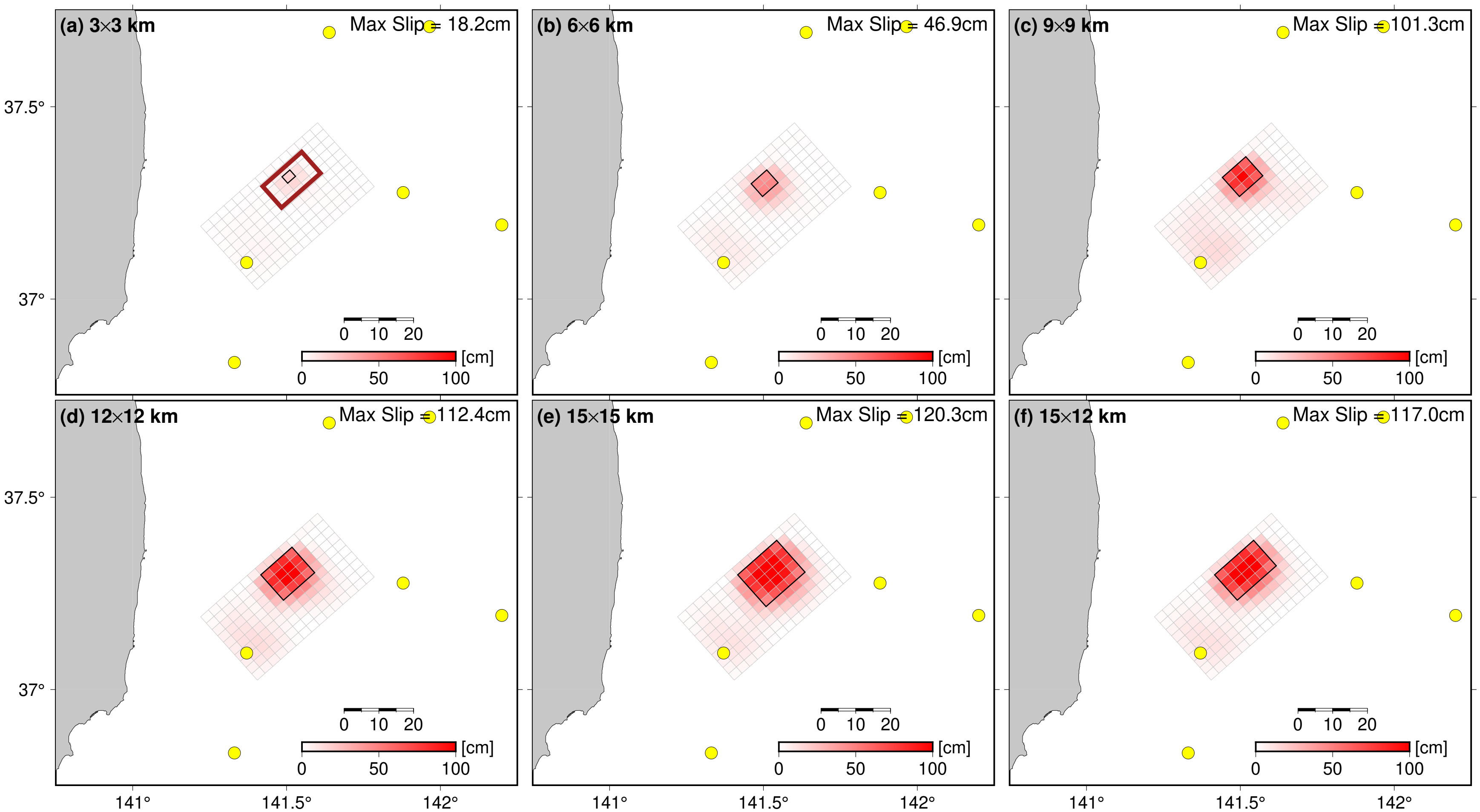

Figure S7. Results of the recovery test of the inversion analysis. The assumed faults sizes are (a) 3 × 3 km, (b) 6 × 6 km, (c) 9 × 9 km, (d) 12 × 12 km, (d) 15 × 15 km, and (e) 15 × 12 km, respectively. The recovered slip distribution is shown by colors, and black rectangles denote the location of the assume fault.

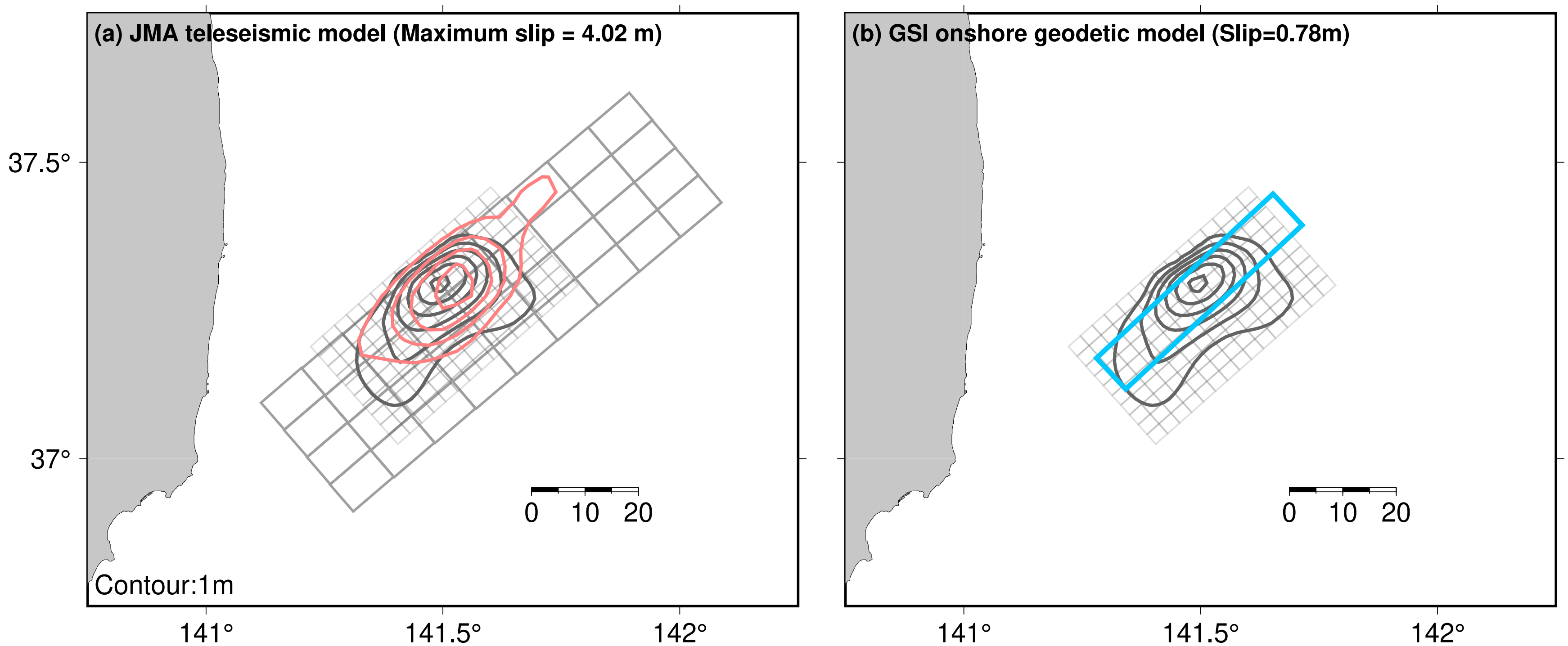

Figure S8. Comparison with the fault model estimated from the onshore data. (a) Comparison with the fault model obtained by using the teleseismic data provided by JMA (https://www.data.jma.go.jp/svd/eqev/data/sourceprocess/event/2016112205594689far.pdf). The gray and pink contour lines denote the slip distribution of the 2016 off-Fukushima earthquake obtained by this study and JMA, respectively (contour interval: 1 m). Large dark gray rectangles show the configuration of the fault plane of the JMA analysis.
(b) Comparison with the fault model obtained by using the onshore geodetic data provided by Geospatial Information Authority of Japan (GSI, https://cais.gsi.go.jp/YOCHIREN/activity/214/214.e.html, https://cais.gsi.go.jp/YOCHIREN/activity/214/image214/008.pdf). The blue rectangle denotes the location of the rectangular planar fault model estimate by GSI. The parameters are follows: fault left top corner location = (37.17°N, 141.28°E, 2.2km), length = 45.1 km, width = 17.7 km, strike = 47.6°, dip = 63.2°, rake = –89.8°, and slip amount = 0.78 m.

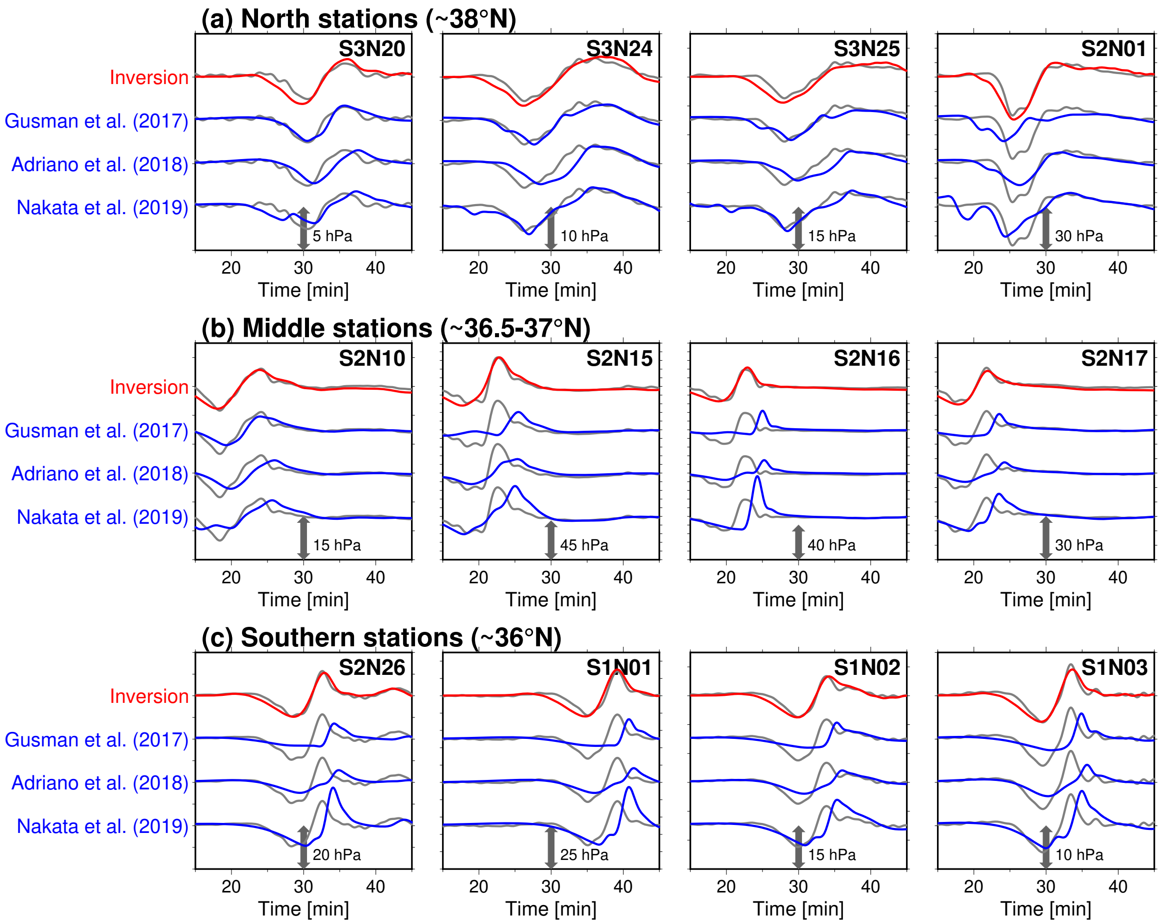

Figure S9. Comparison of the observed (gray) and synthesized S-net OBPG waveforms, from the fault models estimated by this study (red) and the previous studies (blue, Gusman et al., 2017; Adriano et al., 2018; Nakata et al., 2019). (a) Comparison for the stations at northern part of the off northeastern Japan (~38 °N). (b) Comparison for the stations at middle part of the off northeastern Japan (~36.5–37 °N). (c) Comparison for the stations at middle part of the off northeastern Japan (~36 °N).

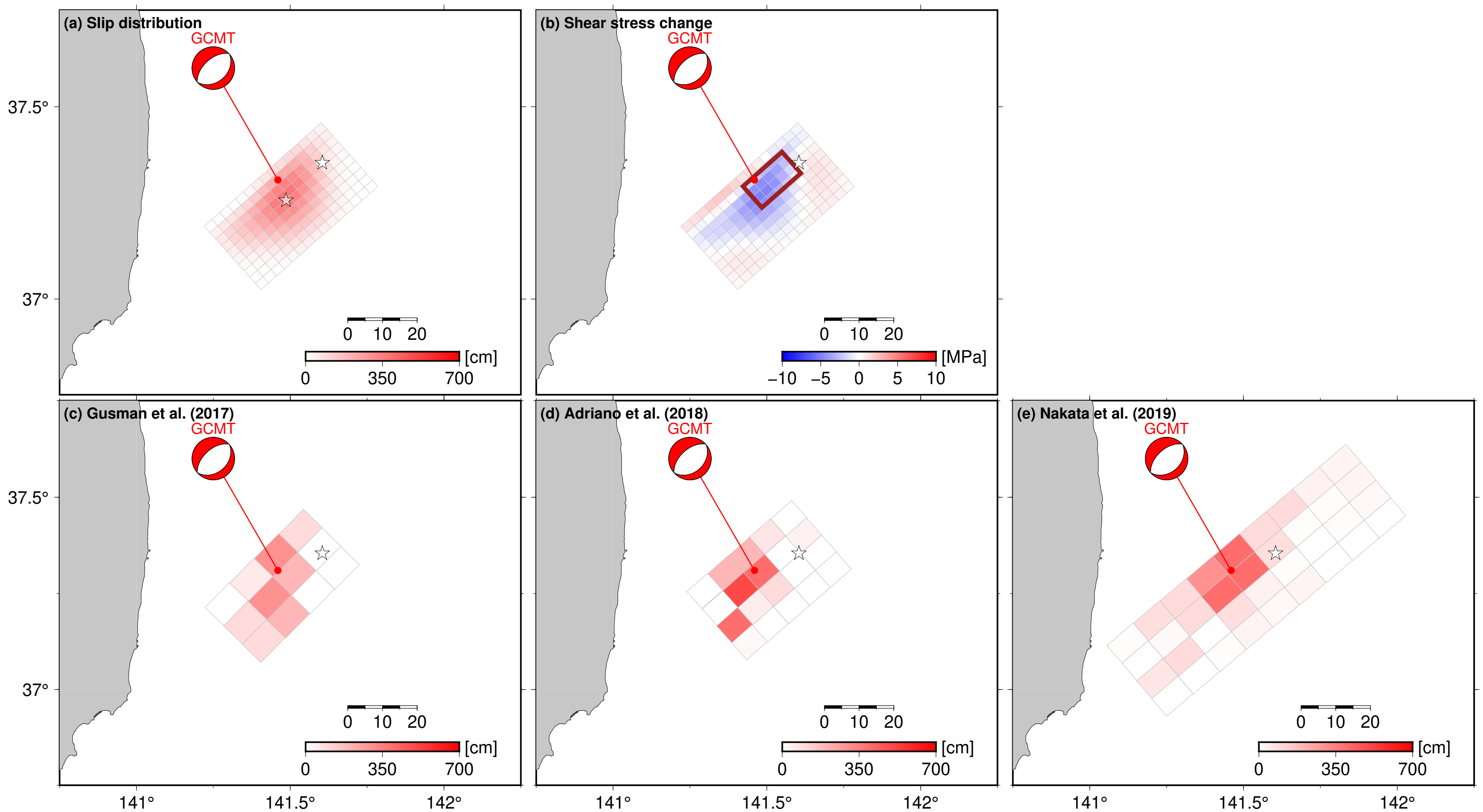

Figure S10. Result of the slip inversion using only the stations far from the focal area. (a) Slip distribution (colored tiles). The pink and white stars indicate the slip-weighted averaged centroid and the JMA epicenter, respectively. (b) Shear stress change along the fault. Negative (blue) and positive (red) denote the shear stress decrease and increase, respectively. The dark red rectangle denotes the optimum rectangular fault obtained by the grid-search analysis. (c–e) Slip distribution by the previous studies.

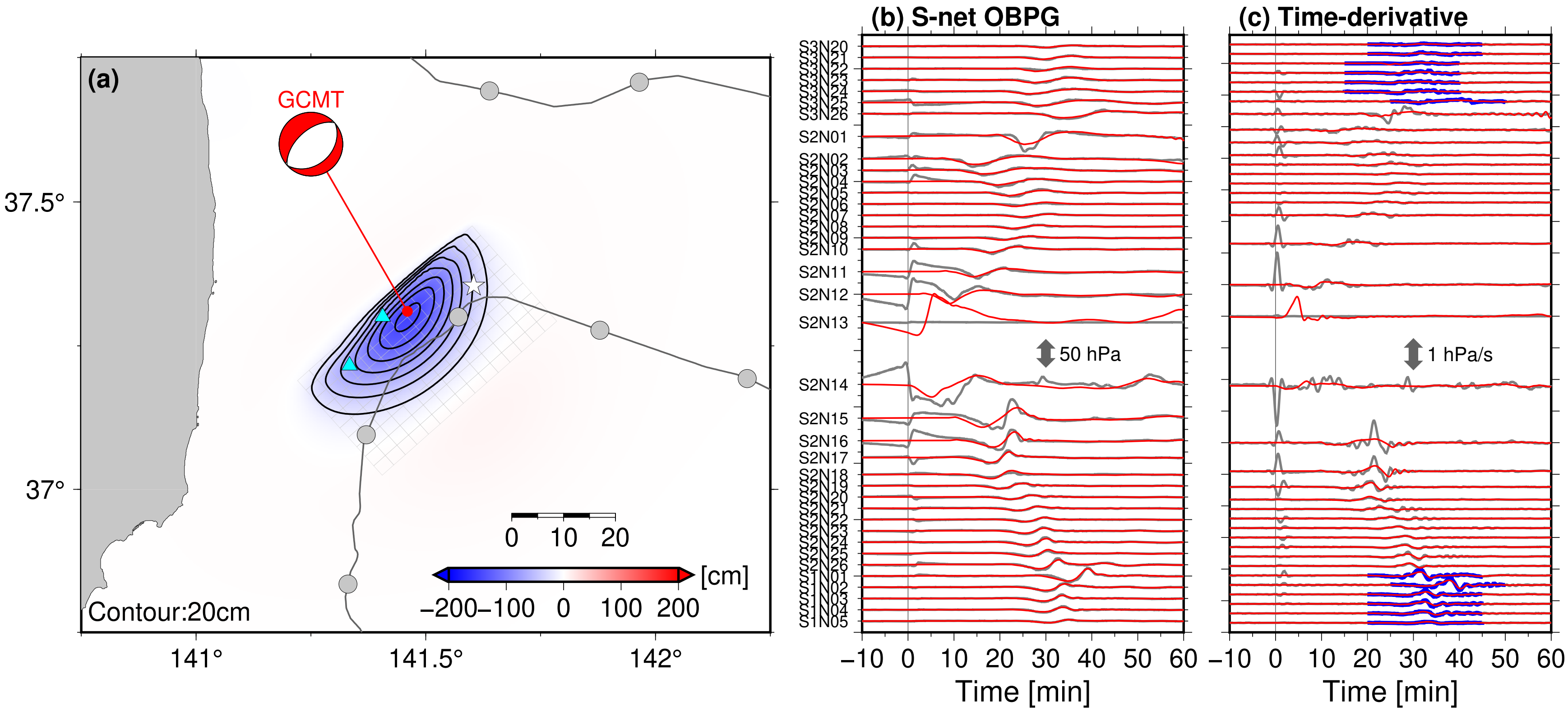

Figure S11. Result of the slip inversion using only the stations far from the focal area. (a) Slip distribution (colored tiles) and tsunami source distribution (black contours, 20 cm interval). (b–c) Comparisons of the observed (gray) and simulated (red) waveforms.

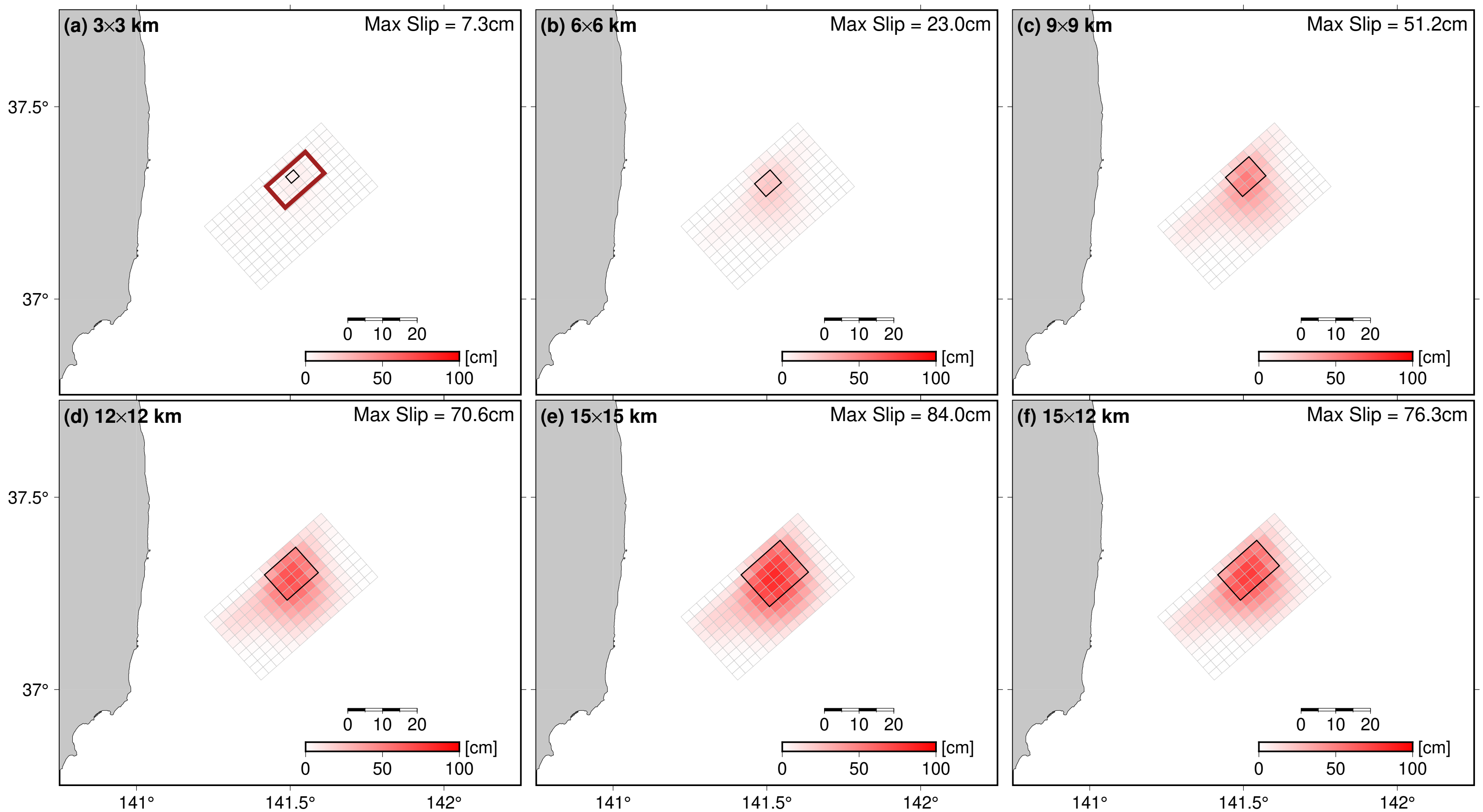

Figure S12. Result of the recovery test, which used only the stations far from the focal area (Figure S10). The other caption is identical to Figure S7.

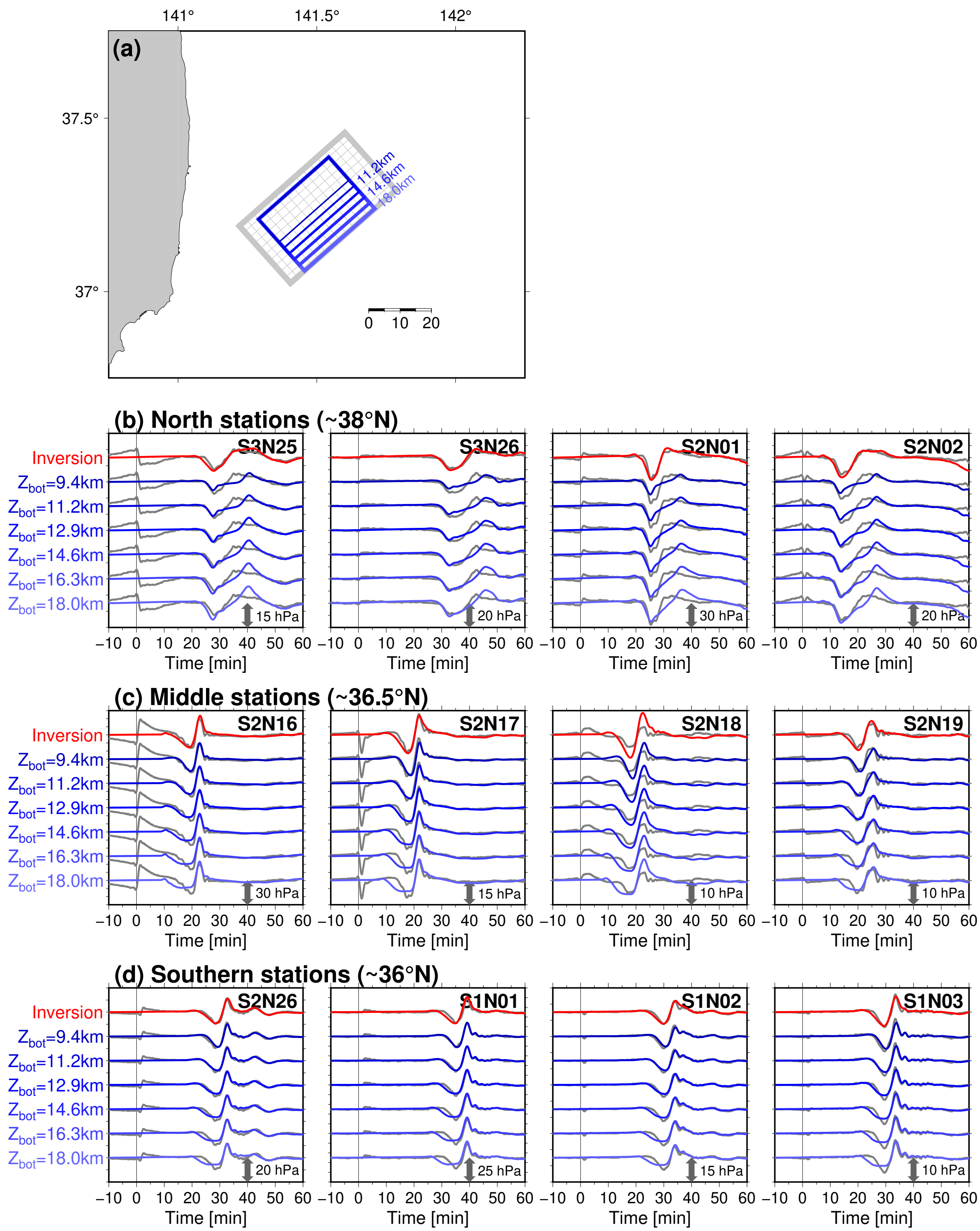

Figure S13. The simulation of the simple rectangular fault with different fault widths. (a) Configurations of the assumed faults. Depths of the bottom end of the rectangular faults (Z_{bot}) are 9.4, 11.2, 12.9, 14.6, 16.3, and 18.0 km. (b–d) Comparisons of the observed (gray) waveforms and the waveforms simulated from the finite fault model (red) and simulated from the assumed rectangular fault models (blue).

Table S1. Time window range used for the inversion analysis.

Station	Begin time of time window [s][a]	End time of time window [s][a]	dt [s]
S3N20	1200	2700	10
S3N21	1200	2700	10
S3N22	900	2400	10
S3N23	900	2400	10
S3N24	900	2400	10
S3N25	900	2400	10
S3N26	1500	3000	10
S2N01	900	2400	10
S2N02	300	1800	10
S2N03	600	2100	10
S2N04	600	2100	10
S2N05	900	2400	10
S2N06	900	2400	10
S2N07	900	2400	10
S2N08	600	2100	10
S2N09	600	2100	10
S2N10	600	2100	10
S2N11	300	1800	10
S2N12	150	1650	10
S2N13	N/A	N/A	N/A
S2N14	150	1650	10
S2N15	600	2100	10
S2N16	600	2100	10
S2N17	600	2100	10
S2N18	600	2100	10
S2N19	600	2100	10
S2N20	600	2100	10
S2N21	900	2400	10
S2N22	900	2400	10
S2N23	900	2400	10
S2N24	900	2400	10
S2N25	900	2400	10
S2N26	900	2400	10
S1N01	1500	3000	10
S1N02	1200	2700	10
S1N03	1200	2700	10
S1N04	1200	2700	10
S1N05	1200	2700	10

[a]Time window is measure from the origin time.
[b]In the inversion, the bandpass-filtered (100–3600 s) data are resampled every *dt* s when solving the observation equation.

Table S2. Search range for the grid search analysis.

Parameters	Range	Increment
Longitude [ab]	141.46°E ± 20 km	5 km
Latitude [ab]	37.31°N ± 20 km	5 km
Depth [ab]	12.0 km ± 10 km[a]	2 km
Strike [a]	49°	Fixed
Dip [a]	35°	Fixed
Rake [a]	−89°	Fixed
Length[c]	5 km – 60 km	5 km
Width[c]	5 km – 60 km	5 km
Slip amount	Adjusted so that the VR value takes the maximum	

[a]Reference values are taken from the GCMT solution.
[b]Fault center location is shown.
[c]When the depth of the updip end of the fault is shallower than a depth of 0.1 km, the calculation is skipped.

Table S3. Station list of the OBPGs installed by Tohoku University

Station	Longitude (°E)	Latitude (°N)	Depth (m)	Observation duration (yyyy/mm/dd)	Logger type[a]
G01	144.9204	38.7030	5456	2016/05/22 – 2017/04/11	UME
G12	143.5317	38.0213	4366	2016/05/24 – 2017/04/10	UME
G16	143.0470	37.3324	4414	2016/05/27 – 2017/04/15	HAK
G17[b]	142.7123	36.8979	4232	2016/05/28 – 2017/04/09	HAK
G19	142.6735	36.4931	5691	2016/05/28 – 2017/04/09	HAK
AoA50	142.3176	36.8725	2853	2016/09/22 – 2017/11/09	UME
AoA60[b]	142.7140	36.8993	4225	2016/09/22 – 2017/10/15	UME
AoA70	142.2868	36.6937	2544	2016/09/22 – 2017/10/15	HAK
FKOB1	142.5800	36.8055	4550	2016/09/28 – 2017/10/15	UME
FKOB2	142.8553	36.7225	5506	2016/09/28 – 2017/10/14	HAK
G15	143.5215	37.6773	5239	2016/10/02 – 2017/10/19	UME

[a]UME: Paroscientific Series 8CB intelligent type pressure sensor + Umezawa-Musen Co. data logger, HAK: Paroscientific Series 8B pressure sensor + Hakusan Co. LS9150 data logger
[b] Station G17 and AoA60 are installed at almost identical location.